Plasmodesmata act as unconventional membrane contact sites regulating inter-cellular molecular exchange in plants

Jessica Pérez-Sancho#[1], Marija Smokvarska#[1], Gwennogan Dubois#[2], Marie Glavier[1], Sujith Sritharan[3], Tatiana Souza Moraes[1], Hortense Moreau[1], Victor Dietrich[1], Matthieu Pierre Platre[4], Andrea Paterlini[1,5,6], Ziqiang Patrick Li[1], Laetitia Fouillen[1], Magali S. Grison[1], Pepe Cana-Quijada[1], Françoise Immel[1], Valerie Wattelet[1], Mathieu Ducros[7], Lysiane Brocard[7], Clément Chambaud[1,7], Yongming Luo[8,9], Priya Ramakrishna[10,11], Vincent Bayle[2], Linnka Lefebvre-Legendre[10], Stéphane Claverol[12], Matej Zabrady[13,14], Wolfgang Busch[4], Marie Barberon[10], Jens Tilsner[13,14], Yrjö Helariutta[5,15], Eugenia Russinova[8,9], Antoine Taly[3], Yvon Jaillais[2]*, Emmanuelle M. Bayer[1,16]*.

[1] Laboratoire de Biogenèse Membranaire, UMR5200, CNRS, Université de Bordeaux, Villenave d'Ornon, France.
[2] Laboratoire Reproduction et Développement des Plantes, Université de Lyon, ENS de Lyon, UCB Lyon 1, CNRS, INRA, F-69342 Lyon, France.
[3] Laboratoire de Biochimie Théorique, UPR9080, CNRS, Université Paris Cité, Paris, France.
[4] Salk Institute For Biological Studies, Plant Molecular and Cellular Biology Laboratory, 10010 North Torrey Pines Road, La Jolla, CA 92037, USA.
[5] The Sainsbury Laboratory, University of Cambridge, Cambridge, UK.
[6] Present address: Institute of Molecular Plant Sciences, School of Biological Sciences, University of Edinburgh, Edinburgh EH9 3BF, UK.
[7] Bordeaux Imaging Centre, Plant Imaging Platform, UMS 3420, INRA-CNRS-INSERM-University of Bordeaux, Villenave-d'Ornon, France.
[8] Department of Plant Biotechnology and Bioinformatics, Ghent University, 9052 Ghent, Belgium.
[9] Center for Plant Systems Biology, VIB, 9052 Ghent, Belgium.
[10] Department of Plant Sciences, University of Geneva, 1211 Geneva, Switzerland
[11] Present address: Laboratory for Biological Geochemistry, School of Architecture, Civil and Environmental Engineering, Ecole Polytechnique Fédérale de Lausanne (EPFL), CH-1015, Lausanne, Switzerland.
[12] Univ. Bordeaux, Bordeaux Proteome, Bordeaux, France
[13] Biomedical Sciences Research Complex, University of St Andrews, Fife KY16 9ST, UK
[14] Cell and Molecular Sciences, The James Hutton Institute, Dundee DD2 5DA, UK
[15] Institute of Biotechnology, HiLIFE/Organismal and Evolutionary Biology Research Programme, Faculty of Biological and Environmental Sciences, Viikki Plant Science Centre, University of Helsinki, Helsinki, Finland.
[16] Lead contact: **emmanuelle.bayer@u-bordeaux.fr** (E.M.B.)

 # These authors equally contributed to the work
*** Correspondence: yvon.jaillais@ens-lyon.fr** (Y.J.), **emmanuelle.bayer@u-bordeaux.fr** (E.M.B.)

In brief

Plant intercellular communication is regulated via tubular membrane contact through PI4P binding-ER-PM tether MCTP proteins

Highlights (4 highlights / 85 characters max)

1- Plasmodesmata are unconventional ER/PM tubular contact sites located at cell-cell interface

2- Plasmodesmata operate as control valves, modulating ER-PM contacts to regulate transport

3- MCTP3, MCTP4, MCTP6 and PI4P tethering elements act as valve regulators

4- SAC7 PI4P phosphatase controls plasmodesmata MCS in a cell-type-specific manner

SUMMARY

Membrane contact sites (MCS) are fundamental for intracellular communication, but their role in intercellular communication remains unexplored. We show that in plants, plasmodesmata communication bridges function as atypical endoplasmic reticulum (ER)-plasma membrane (PM) tubular MCS, operating at cell-cell interfaces. Similar to other MCS, ER-PM apposition is controlled by a protein-lipid tethering complex, but uniquely, this serves intercellular communication. Combining high-resolution microscopy, molecular dynamics, pharmacological and genetic approaches, we show that cell-cell trafficking is modulated through the combined action of Multiple C2 domains and transmembrane domain proteins (MCTP) 3, 4, and 6 ER-PM tethers, and phosphatidylinositol-4-phosphate (PI4P) lipid. Graded PI4P amounts regulate MCTP docking to the PM, their plasmodesmata localization and cell-cell permeability. SAC7, an ER-localized PI4P-phosphatase, regulates MCTP4 accumulation at plasmodesmata and modulates cell-cell trafficking capacity in a cell-type specific manner. Our findings expand MCS's functions in information transmission, from intracellular to intercellular cellular activities.

INTRODUCTION

Recent years have seen a paradigm shift in our understanding of intracellular communication with the discovery of membrane contact sites (MCS) (Scorrano et al., 2019; Prinz et al., 2020). By mediating close contacts between two membranes, MCS act as specialized platforms for inter-organellar exchanges, enabling transfer of ions and other molecules (Soboloff et al., 2006; Mesmin et al., 2013; Schauder et al., 2014; Chung et al., 2015; von Filseck et al., 2015; Eden et al., 2016; Wong et al., 2016; Wilhelm et al., 2017; Balla, 2018; Bian et al., 2018; Kumagai and Hanada, 2019; Ruiz-Lopez et al., 2021; Qian et al., 2022; Radulovic et al., 2022; Guillén-Samander and De Camilli, 2023; Naón et al., 2023; Wozny et al., 2023). This direct molecular transfer between organelles involves specialized protein machinery and membrane proximity regulation (Scorrano et al., 2019). Interest in MCS has grown dramatically in the last decade, with a shift of focus from describing their molecular composition to understanding their functions. Besides inter-organellar communication, MCS were shown to be involved in organelle biogenesis, fission and trafficking, cargo sorting, cellular stress responses, and autophagy; highlighting the functional diversity of these eukaryotic structures (Eden et al., 2010; Friedman et al., 2011; Hamasaki et al., 2013; Rowland et al., 2014; Pérez-Sancho et al., 2015a; Dong et al., 2016; Hirabayashi et al., 2017; Lees et al., 2017; Collado et al., 2019; Hernández-Alvarez et al., 2019; Hoffmann et al., 2019; Lee et al., 2019a; Wang et al., 2019; Ruiz-Lopez et al., 2021). It is now clear that every organelle inside a single cell forms functional contacts, and that MCS activities are not only broad but also vital for the cell. While MCS are now well-established and essential contributors to intracellular coordination, many multicellular eukaryotic organisms require effective communication that extends beyond organelles and includes communication between individual cells. So far, our understanding of MCS function is restricted to intracellular activities, and there is currently no evidence supporting the notion that MCS facilitate direct molecular exchange between cells.

With this shift in mind, we addressed the possible functions of MCS in inter-cellular (as opposed to inter-organellar) molecular exchange. Among eukaryotic cells, the endoplasmic reticulum (ER) serves as a central hub for MCS, forming multiple contacts with various organelles(Salvador-Gallego et al., 2017; Wu et al., 2018a). In most eukaryotic cells the ER is confined to a single cell. However, in land plants and some green algae, the ER network extends from cell-to-cell through communication bridges known as plasmodesmata (Nicolas et al., 2017b) (**Figure 1A**). Unlike desmosome cell-cell junctions or any other cell-cell contact dependent communication structures, both the ER and the PM traverse cell-cell boundaries through plasmodesmata. Inside plasmodesmata the ER takes the form of a condensed membrane tube known as the desmotubule which comes in close apposition with the PM, creating an atypical tubular MCS-like structure (Ding et al., 1992; Tilsner et al., 2016; Nicolas et al., 2017a). Millions of plasmodesmata bridges weave through the plant body, allowing direct molecular exchange of nutrients and signaling molecules in the space between the ER and the PM, called the cytoplasmic sleeve (Deinum et al.,

2019) (**Figure 1A**). These structures are pivotal for plant intercellular communication, allowing cells to coordinate their activities, exchange resources, and respond to environmental and developmental signals in a synchronized manner (Nakajima et al., 2001; Guseman et al., 2010; Benitez-Alfonso et al., 2013; Faulkner et al., 2013; Stahl et al., 2013; Wang et al., 2013; Daum et al., 2014; Vaddepalli et al., 2014; Otero et al., 2016; Stahl and Faulkner, 2016; Gaudioso-Pedraza et al., 2018; Tylewicz et al., 2018; Miyashima et al., 2019; Song et al., 2019; Tran et al., 2019; Gao et al., 2020; Mellor et al., 2020; Kitagawa et al., 2022; Mehra et al., 2022; Tee et al., 2022; Wang et al., 2023). Yet the molecular mechanisms regulating cell-cell molecular flow continue to evade complete understanding.

While plasmodesmata comply with the general definition of MCS: (1) area of close proximity between two membranes, (2) absence of membrane fusion, (3) site of specialized function and (4) defined proteome and lipidome (Li et al., 2021), we still do not know if they function as MCS. Their unique membrane organization has been known for decades and yet it is still not known whether plasmodesmata-driven cell-cell communication requires regulation of ER-PM contacts and if dysregulation of these contacts impacts the functionality of plasmodesmata. Until now, the local synthesis and degradation of a beta-1,3-glucan polymer (callose) in the wall around plasmodesmata, is the only characterized mechanism to regulate plasmodesmata permeability (Zavaliev et al., 2011; Amsbury et al., 2017; Wu et al., 2018b). Additionally, plant viruses also encode movement proteins, which can also act as exogenous regulators of plasmodesmata permeability to transfer the viral genome through plasmodesmata (Crawford and Zambryski, 2001; Guenoune-Gelbart et al., 2008; Amari et al., 2010; Tilsner et al., 2013; Tilsner et al., 2014).

Given their position at cell-to-cell interfaces, we hypothesize that regulating ER-PM contact sites at plasmodesmata may function as a mechanism to modulate the diffusion of cytoplasmic components between neighboring cells. This mechanism would stand as the first example in eucaryotes of MCS driven-intercellular communication. In this work, we undertook to identify the molecular actors by which plasmodesmata may control the exchange of information among cells by regulating MCS, with a focus on the model plant *Arabidopsis thaliana.*

RESULTS

MCTP3, MCTP4 and MCTP6 form a tethering complex at plasmodesmata and redundantly impact plant growth and development

Plasmodesmata are dynamic nanoscopic structures with the capacity to dilate and contract, acting as checkpoints controlling cell-to-cell trafficking. Sitting at the cell-cell interface, they have the potential to combine membrane contact regulation with intercellular functions. In this scenario, MCS would act as a valve, controlling molecular flow by adjusting the ER-PM gap and/or changing the cytoplasmic sleeve property through steric hindrance (**Figure 1A**). To test this

148 hypothesis, we first targeted the molecular machinery controlling ER-PM contact. MCS are
149 regulated by protein tethers which physically bridge the two membranes (Scorrano et al., 2019).
150 Previously, we identified members of the Multiple C2 domains and transmembrane domain
151 proteins (MCTPs) family as putative plasmodesmata tethers (Brault et al., 2019). Besides, Miras
152 et al. (Miras et al., 2022b) identified MCTPs among 20 core plasmodesmata proteins by cross-
153 referencing the proteomes of *Arabidopsis thaliana*, *Populus trichocarpa*, and *Nicotiana*
154 *benthamiana*. Johnston *et al.* (Johnston et al., 2023) also classified them as one of three conserved
155 plasmodesmata families through phyloproteomics.

156

157 We therefore selected MCTPs as ER-PM tether candidates and evaluated their function in cell-cell
158 trafficking in the model plant *Arabidopsis thaliana*. MCTPs are structurally related to the MCS
159 tethers Extended-synaptotagmins (E-Syts) in animal and Synaptotagmins (SYTs) in plant
160 (Giordano et al., 2013; Pérez-Sancho et al., 2015a; Brault et al., 2019; Ruiz-Lopez et al., 2021).
161 They consist of a C-terminal ER-anchor and three to four C2 lipid binding domains (**Figure 1B**).
162 Nearly all plant cells are interconnected by plasmodesmata, so a primary component is expected
163 to be widely expressed and consistently associated with them, regardless of tissue type or
164 developmental stage. In Arabidopsis, the MCTP family comprises 16 members, among which
165 MCTP3, MCTP4, and MCTP6 were identified in plasmodesmata fractions in a systematic manner
166 (Fernandez-Calvino et al., 2011; Kraner et al., 2017; Brault et al., 2019; Kirk et al., 2022; Miras et
167 al., 2022a; Gombos et al., 2023; Johnston et al., 2023). Analysis of publicly available gene
168 expression profiling databases revealed that all three genes were widely and consistently expressed
169 in both shoot and root tissues, with MCTP4 exhibiting the strongest expression levels (**Figure S1A**
170 **and S1B**). In all examined tissues, the proteins displayed a dotty localization at cell-cell interfaces,
171 reminiscent of plasmodesmata (**Figure 1B; Figure S1C-E; Movie S1-3**). All three members show
172 plasmodesmata association when expressed under their endogenous promoters as confirmed by
173 Airyscan imaging and co-localization with callose, a well-established plasmodesmata marker
174 (**Figure S1F;** Brault et al. 2019). MCTP3, 4 and 6 can physically interact when co-expressed as
175 shown by co-immunoprecipitation when transiently expressed (**Figure S2A-B**). The interaction at
176 plasmodesmata was confirmed using Förster Resonance Energy Transfer Fluorescence Lifetime
177 Imaging Microscopy (FRET-FLIM) analysis with functional pMCTP4::TagRFP-MCTP4 co-
178 expressed with pMCTP3::eYFP-MCTP3 in the complemented triple mutant background *mctp3-*
179 *1/mctp4-1/mctp6-1* (**Figure S2C**).

180

181 Single loss-of-function mutants (*mctp3-1*, *mctp3-2, mctp4-1, mctp4-2* or *mctp6-1*) presented no
182 strong phenotypic anomaly (**Figure S2D-E, S3)**. However, the double mutants involving MCTP4
183 loss-of-function (*mctp3-1/mctp4-1, mctp3-2/mctp4-1, mctp4-1/mctp6-1*) were severely affected in
184 both shoot and root growth and development (**Figure S2D-E, S3**). The triple *mctp3-1/mctp4-*
185 *1/mctp6-1* mutant was not viable when grown on soil and died after two weeks (**Figure S3)**. The
186 strong pleiotropic phenotype is consistent with a role in the coordination of cellular activity at the
187 multicellular level.

188
189 Altogether, these data indicate that MCTP3, MCTP4, and MCTP6 are core plasmodesmata
190 constituents making them suitable targets for investigating plasmodesmata MCS function.
191

192 **MCTPs act as ER/PM tethers inside plasmodesmata bridges, controlling membrane contact**

193 In previous work, we showed that overexpressing MCTP4 in a delta-ER-PM tether yeast
194 mutant partially restored cortical ER, suggesting a potential function as membrane tether (Brault
195 et al., 2019). To test whether MCTP3, MCTP4 and MCTP6 act as ER-PM linkers inside
196 plasmodesmata, we checked whether their genetic deletion would loosen the ER-PM gap within
197 the bridges.

198 Functional redundancy has been shown for E-Syts and SYTs (Saheki et al., 2016; Lee et al., 2020;
199 Ruiz-Lopez et al., 2021) with only high order mutants showing clear ER-PM detachment
200 (Giordano et al., 2013). Therefore, we focused on *mctp3-1/mctp4-1/mctp6-1* mutant to check for
201 potential plasmodesmata structural defects. We used primary root, which allows high-resolution
202 microscopy imaging of plasmodesmata by electron tomography on high-pressure frozen, freeze-
203 substituted samples (Nicolas et al., 2017a; Yan et al., 2019). Electron tomography is the only
204 technology capable of achieving the nanometer-scale resolution necessary to visualize
205 plasmodesmata, which are only 20-40 nm in diameter. We focused on the root epidermis division
206 zone, where plasmodesmata structure is well preserved after cryo-fixation, and on apical-basal
207 walls where plasmodesmata are highly active in transport (Nicolas et al., 2017a). We adapted our
208 previous protocol (Petit et al.; Nicolas et al., 2017a) to reduce staining and increase substructural
209 resolution (see material and methods for details). This new protocol allowed us to visualize the
210 ER-PM boundary within plasmodesmata and discern potential membrane detachment with more
211 precision, while maintaining excellent cell fixation and structural membrane preservation (**Figure**
212 **S4A**). Altogether we acquired over 80 tomograms of plasmodesmata. While in wild-type plants, a
213 large proportion of plasmodesmata presented tight ER-PM contacts throughout the entire length
214 of plasmodesmata (~70 % plasmodesmata; n=50) as previously described (Nicolas et al., 2017a)
215 (**Figure 1C, Movie S4),** this configuration was lower in the *mctp3-1/mctp4-1/mctp6-1* mutant (~10
216 % plasmodesmata; n=30). Instead, the majority of plasmodesmata in the *mctp3-1/mctp4-1/mctp6-*
217 *1* mutant showed clear and visible ER-PM membrane detachment (~90% of plasmodesmata in
218 *mctp3-1/mctp4-1/mctp6-1* mutant as opposed to ~30% in the wild-type) (**Figure 1C (i) (ii), Figure**
219 **S4B, Movies S5-6**). In some cases (about ~10%), membrane separation in *mctp3-1/mctp4-*
220 *1/mctp6-1* was nearly complete, as illustrated in **Figure S4B (iii)** (**Movie S6**). Furthermore, when
221 measuring the ER-PM distance at detachment points, we observed larger values in the triple *mctp*
222 mutant compared to wild-type (**Figure 1C (iii)**). Average plasmodesmata diameter (PM-PM) was
223 slightly higher *mctp* mutant compared to wild-type (**Figure S4C**) likely due to more frequent ER-
224 PM detachments. These data indicate that MCTP3/MCTP4/MCTP6 act as ER-PM tethers inside
225 the plasmodesmata bridges and that their loss-of-function leads to looser membrane junctions.

226
227 **Loss of MCTP ER-PM tethers increases intercellular molecular flow through**
228 **plasmodesmata**
229
230 We next tested the impact of loss of MCTP tethers on intercellular trafficking. We first
231 used fluorescence recovery after photobleaching (FRAP) on the carboxyfluorescein diacetate
232 (CFDA) cytosolic dye. CFDA is a cell-permeant compound which once loaded in the cells is
233 cleaved by intracellular esterases, creating a membrane-impermeable fluorescent probe that moves
234 from cell-to-cell through plasmodesmata (Nicolas et al., 2017a). After photobleaching in the root
235 division zone, we noted a significantly faster recovery in both *mctp3-2/mctp4-1* and *mctp3-*
236 *1/mctp4-1/mctp6-1* mutants compared to wild-type (**Figure 1D**). No differences were noted in
237 terms of recovery rate between the *mctp3-2/mctp4-1* and *mctp3-1/mctp4-1/mctp6-1* mutants. This
238 could be attributed to MCTP6 down regulation in the *mctp3-2/mctp4-1* mutant background (Brault
239 et al., 2019).To validate that loose ER-PM contacts within plasmodesmata is indeed leading to an
240 increase in molecular flow, we next employed the genetically encoded DRONPA-s, a reversibly
241 switchable photoactivatable fluorescent marker. DRONPA-s is bigger than CFDA with an
242 estimated Stoke radius of 2.8 nm against 0.61 nm for CFDA, allowing us to assess how molecules
243 of different sizes behave. Cytosolic DRONPA-s was selectively activated in a single cell via two-
244 photon excitation microscopy, and movement into neighboring cells monitored over time (Gerlitz
245 et al., 2018). This enabled us to precisely evaluate variations in molecular flow in the apico-basal
246 walls of the root epidermis division zone, where the tomography study was conducted. We selected
247 both the double *mctp3-2/mctp4-1* and the triple *mctp3-1/mctp4-1/mctp6-1* mutants to express
248 cytosolic DRONPA-s. Despite repetitive attempts, we only obtained sufficient DRONPA-s
249 expression levels in the double *mctp3-2/mctp4-1* mutant. After activation of DRONPA-s in one
250 cell (N), its cell-cell transport can be monitored as the loss of DRONPA-s signal in the activated
251 cell or the gain of DRONPA-s in the neighbors (N+1, N+2 and N-1, N-2) over time (**Figure 1E-**
252 **F**). Loss-of-function in *mctp3-2/mctp4-1* resulted in much faster DRONPA-s loss in the activated
253 cell and significantly increased movement in the N±1 neighboring cells (**Figure 1E-F**; **Movie S7**),
254 indicating that plasmodesmata efflux capacity was more permissive than in wild-type plants. This
255 permissive molecular flow was not specific to the epidermis, as both the endodermis and cortex
256 presented a similar pattern (**Figure 1F**). Together these data show that modifying the ER-PM
257 contacts by means of MCTP3/MCTP4/MCTP6 tether complex, modifies plasmodesmata transport
258 capacity.

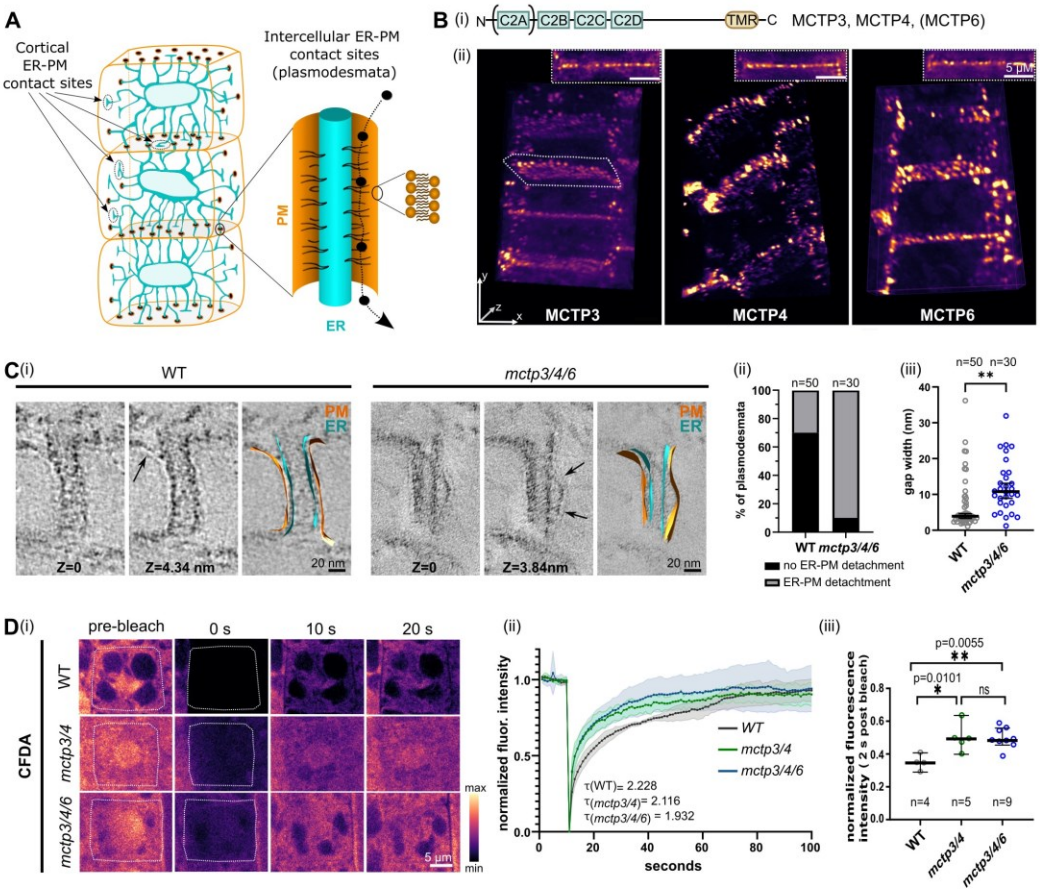
A
Cortical ER-PM contact sites
Intercellular ER-PM contact sites (plasmodesmata)
PM
ER
B (i) N C2A C2B C2C C2D TMR C MCTP3, MCTP4, (MCTP6)
(ii)
5 µm
MCTP3
MCTP4
MCTP6
C (i) WT
mctp3/4/6
PM
ER
Z=0
Z=4.34 nm
Z=3.84nm
20 nm
(ii)
n=50 n=30
% of plasmodesmata
WT mctp3/4/6
no ER-PM detachment
ER-PM detachment
(iii)
n=50 n=30
**
gap width (nm)
WT
mctp3/4/6
D (i)
pre-bleach
0 s
10 s
20 s
CFDA
WT
mctp3/4
mctp3/4/6
max
min
5 µm
(ii)
normalized fluor. intensity
WT
mctp3/4
mctp3/4/6
τ(WT)= 2.228
τ(mctp3/4)= 2.116
τ(mctp3/4/6) = 1.932
seconds
(iii)
p=0.0055
**
p=0.0101
*
ns
normalized fluorescence intensity (2 s post bleach)
n=4 n=5 n=9
WT
mctp3/4
mctp3/4/6
E (i)
before activation
activation
60 s
120 s
p35S::DRONPA-s
WT
mctp3/4
N-2 N-1 N N+1 N+2
5µm
(ii)
fluorescence intensity (a.u)
WT
mctp3/4
distance (pixels)
F (i)
fluorescence to 100 %
seconds
epidermis
cortex
endodermis
mctp3/4
epidermis
cortex
endodermis
WT
(ii)
fluorescence to 100 % at 120sec
p=0.0058
**
p<0.0001
****
p<0.0001
****
n=27 n=47
n=25 n=27
n=28 n=19
WT mctp3/4
epidermis
cortex
endodermis

259

Figure 1. MCTPs function as ER-PM tethers within plasmodesmata and regulate its diffusion capacity.
(A) Schematic representation of ER-PM contact sites in plants.
(B) (i) Schematic representation of plant ER-PM contact site tethers MCTPs depicting phospholipid-binding C2 domains and ER-anchored transmembrane regions (TMR). The size of the domains and the distances between them is not to scale. (ii) 3D view of *mctp3/4 pUBQ10::eYFP MCTP3*, *mctp3/4 pUBQ10::eYFP-MCTP4* and *mctp3/4 pUBQ10::MCTP6-mVenus* acquired with lattice light-sheet microscopy. Insets represent one focal plane from the lattice light-sheet set. In this panel and throughout all the figures in the paper, *mctp3/4* stands for *mctp3-2/mctp4-1* and *mctp3/4/6* stands for *mctp3-1/mctp4-1/mctp6-1*.
(C) (i) Individual tomographic slices and segmented 3D reconstructions of plasmodesmata in wild-type (WT) and *mctp3/4/6*. Arrows pointing to ER-PM detachment. Z are two different planes (ii) Contingency plot of the percentage of plasmodesmata showing ER-PM detachment. (iii) Quantification of the distance between ER and PM in WT and *mctp3/4/6* plasmodesmata at the point where the gap is the widest.
(D) CFDA mobility assay measured by FRAP in root epidermal meristematic cells in WT, *mctp3/4* and *mctp3/4/6*. (i) Representative images before and the indicated time after bleach (the cells used for quantification are surrounded by dotted squares). (ii) Normalized fluorescence intensity over a period of 90 seconds after bleaching. Half-life (τ) of CFDA recovery for each genotype is shown. (iii) Normalized fluorescence intensity 2 seconds after photobleaching. Statistical analysis was done with ANOVA followed by Tukey's test. Experiment was repeated twice with similar results.
(E-F) DRONPA-s mobility assay measured as the diffusion of DRONPA-s signal from one single activated cell by two-photon into the neighboring cells in the longitudinal axis. (E) (i) Representative images of the DRONPA-s signal in WT and *mctp3/4* before activation, at activation and 60 and 120 second post activation. N, activated cell; N±1, direct neighbors; N±2, second level neighbors. Propidium iodide (PI, white) was used to mark cell peripheries. (ii) Signal plot showing raw intensity values from the images in (i). F (i) Normalized fluorescence over time of DRONPA-s averaged from N±1 in meristematic epidermis, cortex and endodermis cells imaged every 15 seconds. Lines indicate mean. Error bars indicate SEM. (ii) Percentage of DRONPA-s normalized fluorescence in the N±1 cells at 120 seconds post activation from (i). At least 6 roots were used per cell type per genotype per experiment. Experiment was repeated 3 times and results were pooled for quantification.
When not differently stated, statistical analysis was done with Student t-text. Lines indicate median. Error bars indicate 95% confidence interval (CI).

Heightened cell-to-cell diffusion in *mctp* mutants is independent of callose deposition

In the text-book model, plasmodesmata cell-cell trafficking is primarily regulated by callose, a beta 1-3 extracellular glucan that is specifically enriched around plasmodesmata and metabolized by plasmodesmata-located enzymes. Callose accumulation reduces cell-cell transport while its degradation increases transport (Amsbury et al., 2017). While the exact mechanism of callose action remains elusive, it is proposed to modulate the size of the cytoplasmic sleeve, by increasing or relaxing pressure on the PM.

We therefore enquired if the enhanced cell-cell molecular flow in *mctp3-2/mctp4-1* and *mctp3-1/mctp4-1/mctp6-1* mutants was caused by decreased callose levels. We first checked if the expression of genes associated with callose regulation at plasmodesmata was modified by performing RNAseq analysis of root extracts. The data indicate that none of the callose-related proteins were mis-regulated in either the single *mctp3-2* or *mctp4-1* mutants, or in the *mctp3-2/mctp4-1* double mutant when compared to wild-type plants (**Figure 2A; Figure S5**). We then performed comparative proteomic analysis to see if callose-related proteins were mis-regulated at

305 the protein level. Total protein extract from wild-type, double and triple *mctp* mutant seedlings
306 were simultaneously analyzed by liquid chromatography–tandem mass spectrometry (LC-
307 MS/MS). For each protein identified, its relative enrichment or depletion in the *mctp* mutants
308 versus wild-type was determined (see M&M for details). We selected the same set of proteins as
309 for the callose-related RNAseq analysis (**Figure 2A**). We observed no significant changes in the
310 callose-related proteins that were detected (**Figure 2B**). We next directly quantified callose levels
311 *in situ* in the root division zone by whole-mount immunolocalization using callose-specific
312 monoclonal antibodies, in the same area used for DRONPA-s cell-cell trafficking assay (**Figure**
313 **2C**). The *mctp* double and triple mutants presented similar accumulation of callose as wild-type
314 plants (**Figure 2D**). From these data, we concluded that the increase of cell-cell trafficking in *mctp*
315 mutants is not caused by a reduction of callose levels.

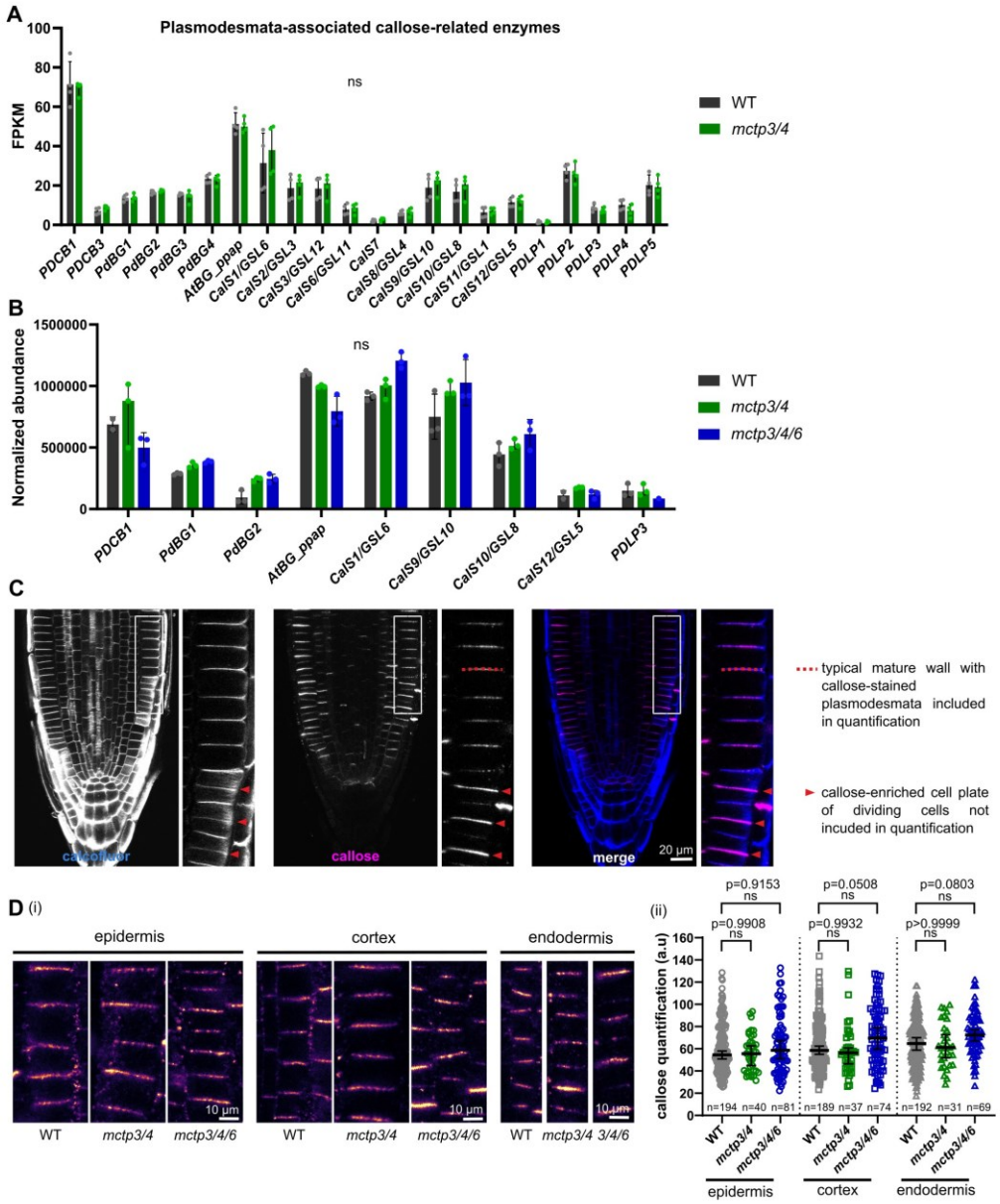

Figure 2. Loss of function of MCTP does not lead to defects in callose deposition

(A) Normalized expression of callose-related enzymes based on mRNA-seq of WT and *mctp3/4*. FPKM, Fragments per kilobase mapped. Bars reach the value of the median. Error bars represent 95% CI. Statistical analysis was done with multiple paired t-test. Experiment includes 4 biological replicates, each of them being a pool of 40 mg of 5 days old roots cut at 1 cm from the tip.

(B) Normalized protein abundance of callose related enzymes based on mass spectrometry of WT, *mctp3/4* and *mctp3/4/6*. Bars reach the value of the median. Error bars represent 95 % CI. Statistical analysis was done with background-based ANOVA. Experiment includes 3 biological replicates, each of them being a pool of 80 mg of 5 days old roots cut at 1 cm from the tip.

(C) Representative images of whole-mount anti-callose immunostaining (magenta) of WT showing the root apical meristem. Calcofluor (blue) was used to stain cell-walls. The white rectangle indicates the area generally used for

quantification. For each mature cell-wall, a segmented line was drawn (dashed-red line as an example) and the mean intensity value along the line was used for quantification. Red arrowheads point to cell-walls that are not included in the analysis because they are just formed, as indicated by a very intense anti-callose signal and weak calcofluor signal. (D) Callose accumulation in the epidermis, cortex and endodermis meristematic cells of WT, *mctp3/4* and *mctp3/4/6*. (i) Representative confocal images of anti-callose immunostaining. (ii) Quantification of callose as explained in (C). Lines indicate median. Error bars indicate 95 % CI. Statistical analysis was done with ANOVA followed by Tukey's test. A minimum of 4 roots were used per genotype, per experiment. Experiment was repeated twice with similar results and data were pooled together.

Defective ER-PM tethering impairs the dynamic control of intercellular molecular flow

Intercellular communication is dynamically controlled, and a key feature of plasmodesmata lies in their ability to respond to various environmental or developmental stimuli by reducing or increasing intercellular molecular flow (Gisel et al., 1999; Faulkner et al., 2013; Han et al., 2014; Cui and Lee, 2016; Cheval and Faulkner, 2018; Gaudioso-Pedraza et al., 2018; Lexy et al., 2018; Tylewicz et al., 2018; Grison et al., 2019; Sager et al., 2020; Mehra et al., 2022; Tee et al., 2022; Wang et al., 2023). We therefore tested whether dynamic regulation of trafficking persisted in the absence of a fully functional tether machinery.

We first tested how plasmodesmata responded to brassinosteroid levels, which are known to modify cell-cell transport and callose deposition (Wang et al., 2023). We used brassinazole, a brassinosteroid biosynthesis inhibitor, which drastically reduces callose levels and promotes cell-cell trafficking (Wang et al., 2023). Upon exposure to brassinazole (24h, 1 µM), wild-type roots exhibited almost complete suppression of callose accumulation (**Figure 3A**). A similar effect was observed in both *mctp3-2/mctp4-1* and *mctp3-1/mctp4-1/mctp6-1* mutants, reaffirming that callose response remains unaffected in the *mctp* mutants (**Figure 3A**). As expected, in wild-type plants, DRONPA-s spread faster into neighboring cells after callose removal (**Figure 3B**). In this condition, cell-cell trafficking in the wild-type increased to the same magnitude as in untreated *mctp3-2/mctp4-1* plants. However, callose removal in the *mctp3-2/mctp4-1* mutant did not change macromolecular flux, which remained identical to control conditions (**Figure 3B**).

Next, we tested if down-regulation of cell-cell trafficking was functional without MCTP tethers, by examining *mctp* mutant responses in conditions known to induce plasmodesmata closure by callose deposition. First, we used brassinolide (Wang et al., 2023) and we confirmed the closure of plasmodesmata upon brassinolide (24h, 200 nM) exposure in wild-type plants, as evidenced by a reduction in DRONPA-s cell-cell diffusion, and callose accumulation (**Figure S6A-B**). In this condition, *mctp* mutants showed an increase in callose identical to the wild-type (**Figure S6B**). However, the impact on cell-cell trafficking was minor and DRONPA-s diffusion remained to the same permissive level in brassinolide-treated *mctp4-1/mctp3-2* mutant than in mock-treated wild-type plants (**Figure S6A)**. Please note that we observed no obvious differences in MCTP4 localisation pattern at cell-cell interface upon brassinosteroid treatments (**Figure S6C).** We next used salt stress (15 min, 20 mM), which triggers short-term callose deposition and plasmodesmata

368 closure (Hunter et al., 2019), as confirmed by quantitative callose immunolocalization and
369 DRONPA-s diffusion (**Figure 3C-D**). Callose deposition was triggered to the same levels in
370 *mctp3-2/mctp4-1, mctp3-2/mctp4-1/mctp6-1* and wild-type roots (**Figure 3C**). However, while
371 wild-type showed sharp decrease in DRONPA-s cell-cell trafficking, plasmodesmata closure was
372 inhibited in *mctp3-2/mctp4-1* mutants (**Figure 3D**).
373
374 Collectively these data indicate that without the MCTP-tether machinery, callose cannot efficiently
375 regulate plasmodesmata. To confirm this, we manipulated callose levels genetically by expressing
376 the gain-of-function callose synthase 3 gene (*cals3m)* (Vatén et al., 2011) under an inducible
377 expression system in the epidermal cells in *mctp3-2/mctp4-1* mutant expressing cytosolic
378 DRONPA-s. After 3h of induction with β-estradiol, we observed a clear accumulation of callose
379 in both the wild-type and *mctp3-2/mctp4-1* mutants (**Figure 3E)**. Cals3m-induced callose
380 deposition translated into a drastic reduction in DRONPA-s cell-cell trafficking in the wild-type
381 but not in the *mctp3-2/mctp4-1* mutant (**Figure 3F, Movie S8)**.
382
383 Altogether, these data indicate that 1) dynamic regulation of cell-cell molecular flow is lost in the
384 absence of functional ER-PM tethers, and 2) callose regulation is no longer effective in *mctp*
385 mutants.

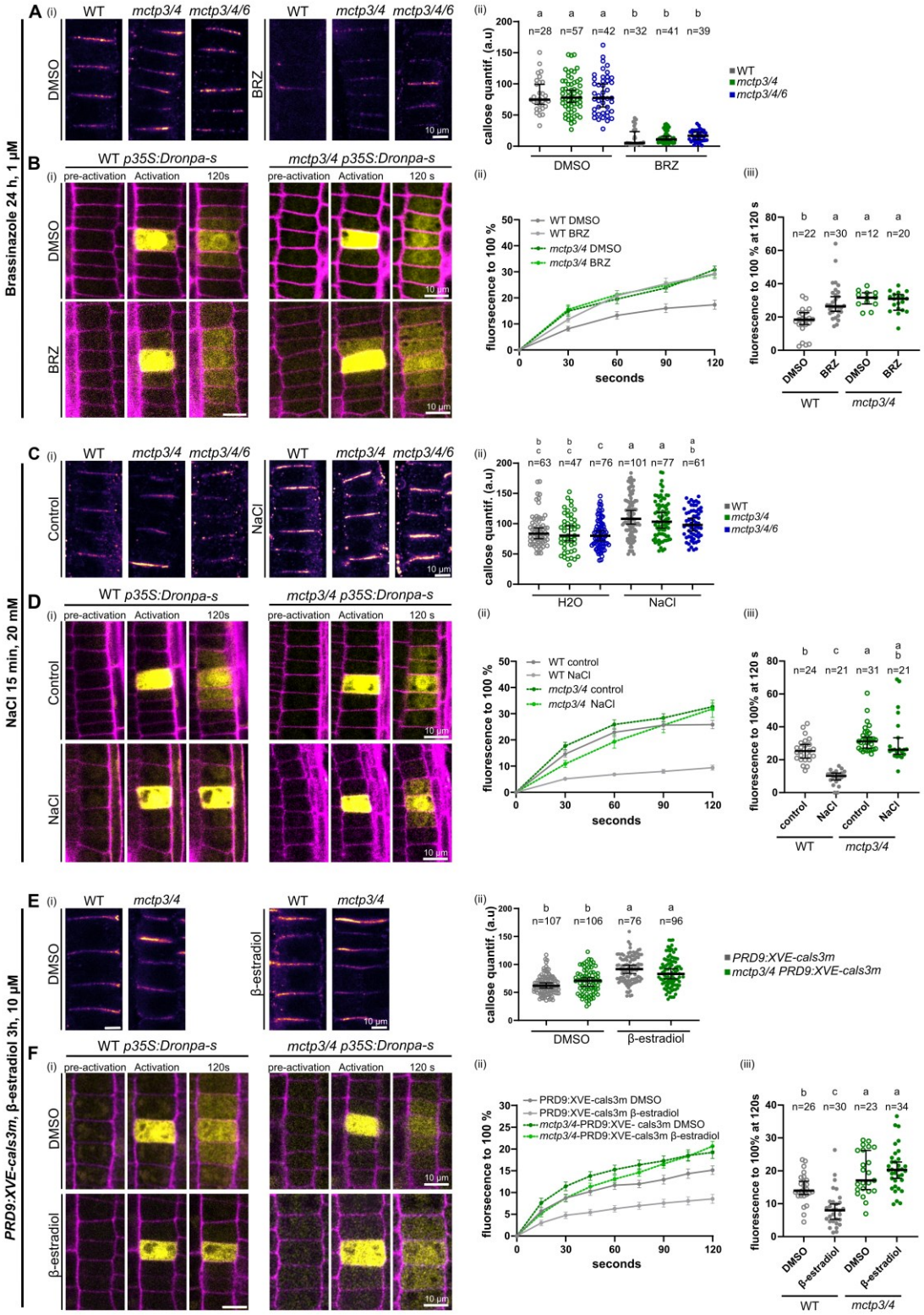
A
(i)
WT
mctp3/4
mctp3/4/6
DMSO
BRZ
10 µm
(ii)
callose quantif. (a.u)
n=28 n=57 n=42 n=32 n=41 n=39
WT
mctp3/4
mctp3/4/6
DMSO
BRZ
Brassinazole 24 h, 1 µM
B
WT p35S:Dronpa-s
mctp3/4 p35S:Dronpa-s
pre-activation
Activation
120s
120 s
(ii)
fluorescence to 100 %
WT DMSO
WT BRZ
mctp3/4 DMSO
mctp3/4 BRZ
seconds
(iii)
fluorescence to 100 % at 120 s
n=22 n=30 n=12 n=20
C
Control
NaCl
n=63 n=47 n=76 n=101 n=77 n=61
H2O
NaCl
NaCl 15 min, 20 mM
D
WT control
WT NaCl
mctp3/4 control
mctp3/4 NaCl
fluorescence to 100% at 120 s
n=24 n=21 n=31 n=21
control
NaCl
E
β-estradiol
n=107 n=106 n=76 n=96
PRD9:XVE-cals3m
mctp3/4 PRD9:XVE-cals3m
PRD9:XVE-cals3m, β-estradiol 3h, 10 µM
F
PRD9:XVE-cals3m DMSO
PRD9:XVE-cals3m β-estradiol
mctp3/4-PRD9:XVE- cals3m DMSO
mctp3/4-PRD9:XVE-cals3m β-estradiol
n=26 n=30 n=23 n=34

386

387 **Figure 3. Callose regulation in loss of function MCTPs has minor effects on the cell-cell diffusion**
388 (A-B) Brassinazole treatment; DMSO or 1 µM Brassinazole (BRZ) for 24 h. (A) Anti-callose immunostaining in
389 treated WT, *mctp3/4* and *mctp3/4/6*. (i). Representative confocal images of callose immunostaining. (ii) Quantification
390 of callose. (B) DRONPA-s mobility assay in treated WT and *mctp3/4*. (i) Representative images of DRONPA-s
391 diffusion. (ii) Normalized DRONPA-s fluorescence over time. Line show mean. Error bars show SEM. (iii).
392 Percentage of DRONPA-s normalized fluorescence in the N±1 cells at 120 s post activation from (ii).
393 (C-D) Salt short-term treatment; H2O (control) or 20mM NaCl for 15 min. (C) Anti-callose immunostaining in treated
394 WT, *mctp3/4* and *mctp3/4/6* (i) Representative confocal images of callose immunostaining. (ii) Quantification of
395 callose. (D) DRONPA-s mobility assay in treated WT and *mctp3/4*. (i) Representative images of DRONPA-s
396 diffusion. (ii) Normalized DONRPA-s fluorescence over time. Line show mean. Error bars show SEM. (iii) Mean
397 percentage of DRONPA-s normalized fluorescence in the N±1 cells at 120 s post activation from (ii).
398 (E-F) Callose-inducible *pPRD9::XVE-cals3m*; DMSO or 10µM b-estradiol for 3 h. (E) Anti-callose immunostaining
399 in treated WT *pPRD9::XVE-cals3m* and *mctp3/4 pPRD9::XVE-cals3m*. (i) Representative confocal images of callose
400 immunostaining. (ii). Quantification of callose. (F) DRONPA-s mobility assay in treated WT *pPRD9::XVE-cals3m*
401 and *mctp3/4 pPRD9::XVE-cals3m*. (i) Representative images of DRONPA-s diffusion. (ii) Normalized DRONPA-
402 s fluorescence over time. Line show mean. Error bars show SEM. (iii) Percentage of DRONPA-s normalized
403 fluorescence in the N±1 cells at 120 s post activation from (ii).
404 When not specified differently, lines indicate median. Error bars indicate 95 % CI. Statistical analysis was done with
405 ANOVA followed by Tukey's test. Different letters indicate $p<0.05$. A minimum of 5 roots were used per genotype,
406 per condition, per experiment. Experiments were repeated three times with similar results and data were pooled
407 together.
408

409 ## PI4P levels control MCTP docking to the PM

410

411 MCTPs are anchored into the ER through their C-terminal transmembrane region, and were
412 proposed to dock to the PM by interacting with anionic phospholipids through their C2-lipid
413 binding domains (Brault et al., 2019) akin to E-Syts and SYTs (Giordano et al., 2013; Pérez-
414 Sancho et al., 2015a; Benavente et al., 2021) **(Movie S9)**. Anionic phospholipids act as signals in
415 membranes and they are involved in development, reproduction and environmental interactions.
416 They are low-abundant lipids, whose concentration can drastically vary depending on the cell types
417 or during stress episodes (Noack and Jaillais, 2020). We therefore wondered if anionic lipids could
418 regulate plasmodesmata, by controlling MCTP interaction with the PM. We focused on PI4P,
419 which was previously identified as a prime determinant of the PM inner leaflet electrostatic
420 signature in plants (Simon et al., 2016a). Earlier studies on individual MCTP C2 domains
421 suggested that PI4P may indeed promote docking to the PM (Brault et al., 2019). To confirm these
422 data, we purified individual C2 domains of the master regulator MCTP4. While C2C and C2D
423 were insoluble after expression in bacteria, we managed to purify C2B. We then performed
424 liposome sedimentation assays with liposomes of different lipidic composition and confirmed
425 preferential binding of MCTP4-C2B to the lipid bilayer in the presence of PI4P (**Figure 4A**). While
426 PI4P is known to be present at the bulk PM, plasmodesmata, as any MCS, display a specialized
427 membrane environment (Li et al., 2021) and it is not known whether they contain phosphoinositide
428 species. We thus purified plasmodesmata from *A. thaliana* cell culture and ran LC-MS/MS
429 analysis. Both PIP and PIP2 species were indeed detected in plasmodesmata fractions (**Figure 4B**).

430 We next addressed the molecular mechanisms underlying PI4P's role in relation to MCTP
431 membrane tethering activity. We turned to molecular modelling and molecular dynamics to obtain
432 near-atomistic structural insights into MCTP4's interaction with the PM, with spatio-temporal
433 resolution. In previous work, we only assessed individual C2 domains (Brault et al., 2019), here
434 we investigated the behavior of the entire MCTP4 cytosolic domain (the full protein but without
435 the C-terminal ER-anchored transmembrane region) in the presence of a PM-like lipid bilayer. We
436 conducted molecular dynamics simulations using the recently introduced Martini 3 coarse-grained
437 force field (Souza et al., 2021; Borges-Araújo et al., 2023) and we employed Alphafold2 for
438 protein structure prediction (Jumper et al., 2021). MCTPs are anchored into the ER via their TMR
439 domain, restricting their 3D orientation relative to the PM plane. In order to focus solely on
440 functionally relevant protein positioning, we restricted movement in the MCTP4 C2 cytosolic
441 domain, so that the C-terminus of the polypeptide (where the TMR normally is) could not face the
442 PM (**Figure 4C**). The structural model for the cytoplasmic part of MCTP4, comprising the three
443 C2 domains, was extracted from (Sritharan et al., 2023) and embedded in a water box with a lipid
444 bilayer mimicking the PM composition, (~70% phosphatidylcholine (PC), 20% Sitosterol, 10%
445 phosphatidylserine (PS)) and 2% PI4P. To check the interactions between MCTP4 and the PM,
446 we analyzed the fluctuating distances between the C2 domains and the lipid bilayer over time
447 **(Figure 4D)** and the distribution of distances as a function of sequence (y axis) and time (x axis)
448 (**Figure 4E).** Interactions with the PM involve multiple docking configurations, wherein
449 combinations of C2/membrane interaction patterns differ, involving either one C2 (C2C **Figure**
450 **4F** state3 or C2D **Figure 4F** state4), two C2s (C2B and C2C) (**Figure 4F** state1), or all three
451 (**Figure 4F** state2) see **Movie S10**. We next evaluated the interaction of the cytoplasmic part of
452 MCTP4 with a PM with varying concentration of PI4P (0%, 2% or 6%). The data indicate that
453 PI4P boosts the frequency of binding between the C2 domains and the PM, implying a role in
454 stabilizing PM docking (**Figure 4G**).
455 We then identified the amino acids that were directly interacting with PI4P lipids. Examining the
456 electrostatic profile of the C2 domains revealed several positively charged regions on their
457 surfaces, mostly associated with lysines (shown in Movie S11 where the green border areas
458 represent lysine residues) known to play a significant role in membrane binding of peripheral
459 proteins (Tubiana et al., 2022). In our simulations with 2% PI4P, these residues showed significant
460 interactions with the lipid bilayer (**Figure S7A**). We concentrated on the C2C domain which
461 presented the highest hit targets and identified five residues (D217, K218, R220, K318, K322)
462 which showed high PI4P-interaction frequency (**Figure 4I and S7B**) and mutated them to reduce
463 their electrostatic potential (**Figure 4H and S7B**) and performed additional simulations. We
464 conducted the simulations without PI4P and with 2% PI4P. As before, when C2C was not mutated,
465 we observed increased protein-membrane contacts in the presence of PI4P (**Figure 4J**). However,
466 after introducing mutations to the selected PI4P-interacting residues within the C2C domain, we
467 observed a trend towards reduced membrane contacts of the C2C domain even in the presence of
468 PI4P. **(Figure 4J)**.

Altogether, our data show that MCTP C2 domains conditionally interact with membranes depending on the concentration of PI4P, a lipid present at plasmodesmata. These findings suggest that PI4P, as a signaling lipid, may regulate the interaction of MCTP with the PM.

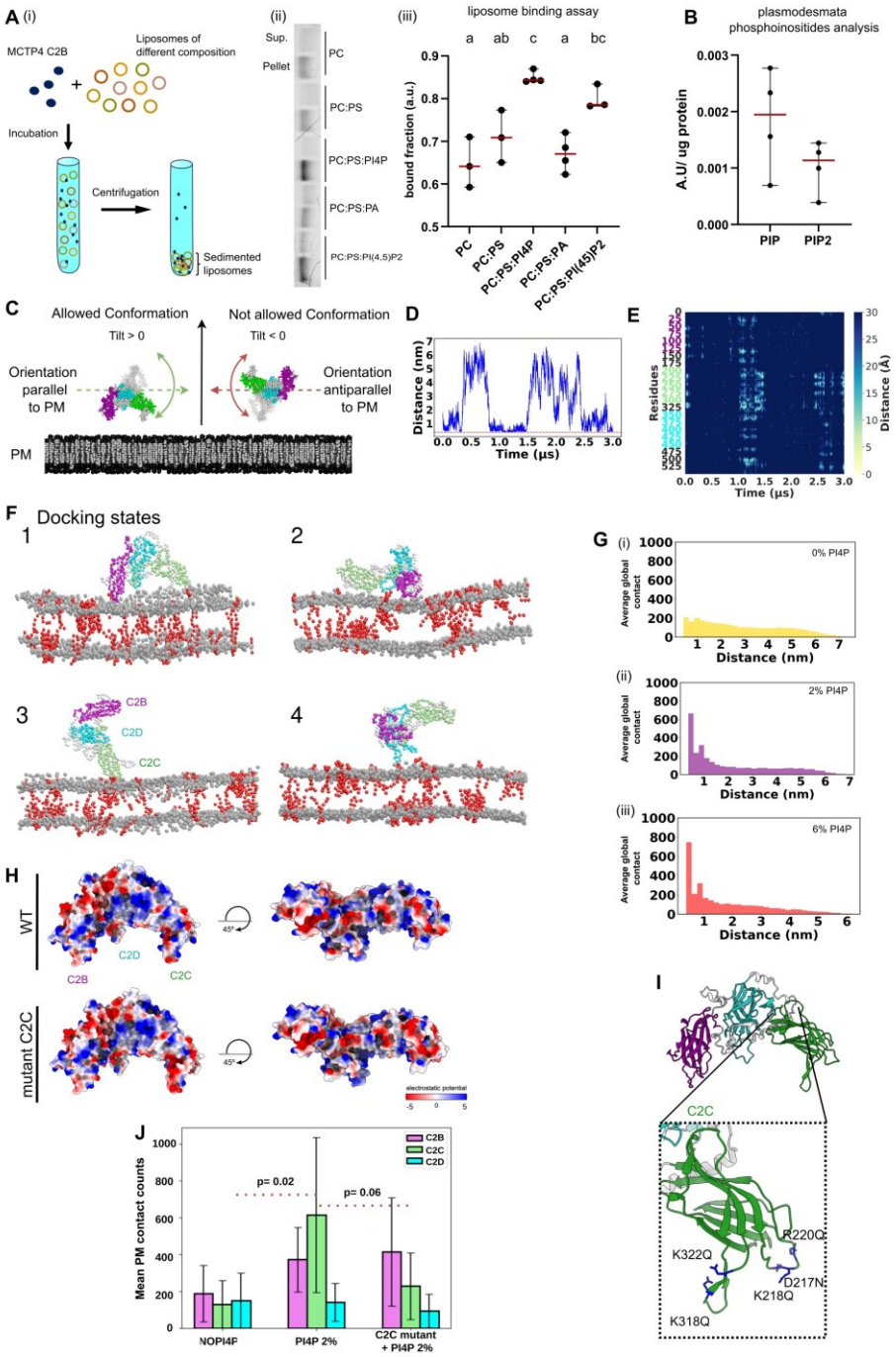

Figure 4. PI(4)P regulates the docking of MCTP4 to the PM by interacting with C2-lipid binding domains

(A) Liposome binding of the purified C2B domain of MCTP4. (i). Schematic representation of the liposome binding assay. Different colors indicate liposomes of different composition. (ii) SDS-PAGE of the supernatant (sup.) and precipitated (pellet) fractions after centrifugation. Proteins were visualized with a Bio-Rad stain-free imager and one single band was observed in each well, corresponding to the C2B domain of MCTP4. (iii) Quantification of the binding of C2B domain of MCTP4 to liposomes of different lipid compositions. Bound fraction was calculated as the ratio between C2B in the pellet and C2B in the supernatant. Line indicates median. Error bars indicate 95% CI. Statistical analysis was done using ANOVA followed by Tukey test. Different letters indicate $p<0.05$. Experiment was repeated 3-4 times and data were pooled together. PC: phosphatidyl choline; PS: phophatidyl serine; PI4P: phosphatidyl inositol 4-phosphate; PA: phosphatidic acid; PI(4,5)P2: phosphatidyl inositol 4,5-biphosphate.

(B) Identification of phosphoinositides in plasmodesmata purified from WT cell cultures. Experiment includes 4 biological replicates.

(C) Application of the Colvar Tilt variable to MCTP4. The harmonic potential activates when the tilt angle is below 0, constraining the system to maintain a realistic orientation relative to the membrane in the absence of the TMR/ER.

(D) Analysis of the minimum distance between the C2 domains and the lipid bilayer over 3 microseconds, illustrating the dynamics of domain-membrane interactions from a single simulation.

(E) Heatmap visualization representing the distances between C2 domain residues and PI4P in the membrane from the same simulation as in (C). The distances are color coded according to the legend in the right.

(F) Snapshots from a simulation of the MCTP4 cytoplasmic domain engaging with a PM-like lipid bilayer in the presence of 2% PI4P: (1) Interaction through two C2 domains, (2) All three C2 domains simultaneously interacting with the bilayer, and (3 & 4) interaction with one different C2 domain.

The simulations lasted 3 microseconds and were repeated 5 times for each condition. The C2 domains appear in different colors: C2B, magenta; C2C, green; C2D, cyan.

(G) Histograms comparing the interaction frequency (average global contact) under three PI4P conditions: without PI4P, with 2% PI4P, and with 6% PI4P, showing increased frequency and stabilization of MCTP4-PM interactions correlating with higher PI4P concentrations.

(H) Surface representation of the C2 block with the electrostatic potential ranging from -5 (red) to 5 (blue), created using ChimeraX. Two different angle-views are used to show the differences between WT block and C2 block with mutated amino acids on the C2C that are putatively responsible for binding with PI4P.

(I) Schematic representation of the C2block (C2B in magenta, C2D in cyan) with a focus on C2C (in green) highlighting the amino acids that were mutated (in dark blue).

(J) Average PM contact counts of the three separate C2blocks in conditions with no added PI4P, 2% PI4P and when putative lipid binding amino acids are mutated on the C2C block in 2% PI4P. Error bars show SD. Data provided by 7 simulations.

MCS modulates cell-cell molecular flow through the tandem action of MCTP tethers and PI4P lipid.

We next tested the impact of PI4P on cell-cell trafficking. Our data supports a scenario where MCTPs bind to the PM through interaction with PI4P. Thus, the removal of PI4P should phenocopy *mctp3-2/mctp4-1* in terms of cell-cell transport capacity. To test this hypothesis, we first assessed the effect of reduced PI4P levels by applying the PI4K inhibitor PAO (phenylarsine oxide) at a concentration and exposure time previously described to affect the localization of PI4P sensors in Arabidopsis roots (Simon et al., 2016) (**Figure 5A**). We then subjected PAO-treated wild-type plants expressing cytosolic DRONPA-s to our cell-cell connectivity test. Inhibiting PI4P synthesis in wild-type plants increased cell-cell trafficking to a similar level than non-treated

520 *mctp3-2/mctp4-1* mutant (**Figure 5A**). By contrast, using YM201636 (an inhibitor of PI(3,5)P_2
521 synthesis) or Wortmannin (an inhibitor of PI3P synthesis) did not change the cell-cell trafficking
522 properties of plasmodesmata (**Figure S8A-C**). We then subjected *mctp3-2/mctp4-1*
523 *p*35S::DRONPA-s to the same PAO treatment. The mutant transport capacity was not affected by
524 PAO (**Figure 5A**), consistent with the notion that MCTP and PI4P act together to regulate
525 plasmodesmata. We also checked that neither PAO nor DMSO differentially affected callose levels
526 in wild-type and *mctp3-2/mctp4-1* mutant backgrounds (**Figure 5B**).
527
528 If PI4P levels are indeed instrumental to the regulation of cell-cell trafficking, elevated PI4P
529 should have the opposite effect than low PI4P and induce plasmodesmata closure. Therefore, we
530 next assayed if increased PI4P level modifies cell-cell transport. To do so, we generated a stable
531 line expressing DRONPA-s in the *suppressor of actin7* (*sac7*, also known as *root hair defective4*)
532 mutant. SAC7 is a PI4P 4-phosphatase, whose mutant accumulates PI4P *in vivo* (Thole et al.,
533 2008; Song et al., 2021). The *sac7* mutant presented reduced DRONPA-s cell-to-cell diffusion,
534 strengthening the idea that PI4P contributes to controlling plasmodesmata connectivity (**Figure**
535 **5C**). Compared to the wild-type, *sac7* has decreased accumulation of callose, ruling out callose as
536 the cause of plasmodesmata closure **(Figure 5D**). We then asked whether callose removal could
537 still open plasmodesmata with increased PI4P levels. Therefore, we treated *p*35S::DRONPA-s
538 lines with brassinazole (24h, 1 µM), which led to callose removal in both wild-type and *sac7*
539 backgrounds (**Figure 5F**). However, while wild-type roots responded by opening plasmodesmata
540 with faster DRONPA-s movement, *sac7* maintained plasmodesmata closed (**Figure 5E**). Thus, the
541 signaling lipid PI4P can modify cell-to-cell cytoplasmic diffusion bypassing callose accumulation,
542 with reduced PI4P levels enhancing molecular movement, and elevated PI4P levels diminishing
543 molecular flow.
544
545 Our data indicate that low PI4P accumulation results in plasmodesmata opening, while high PI4P
546 levels lead to plasmodesmata closure. From these data we concluded that the signaling lipid PI4P
547 may act as a regulator of plasmodesmata connectivity.
548

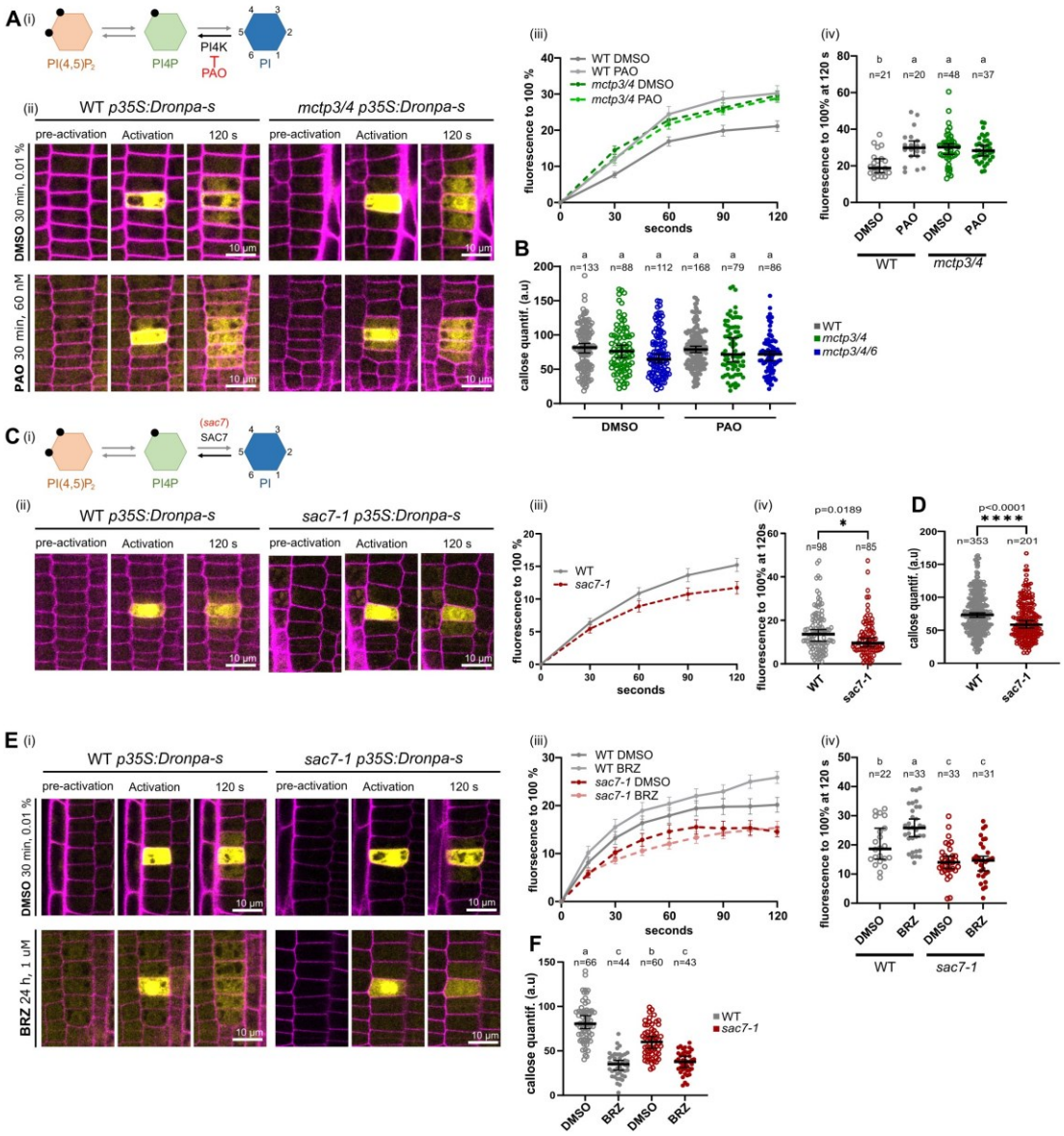

Figure 5: PI4P levels modulate cell-cell molecular flow.

(A-B) PAO treatment; DMSO or PAO 60 nM for 30 min. (A) DRONPA-s diffusion assay in treated WT and *mctp3/4*. (i) Schema of phosphoinositide metabolism depicting the role of PAO blocking PI4K. (ii) Representative images of DRONPA-s diffusion. (iii) Normalized DONRPA-s fluorescence over time. Line indicates mean. Bars show SEM. (iv) Percentage of DRONPA-s normalized fluorescence in the N±1 cells at 120 seconds post activation from (iii). (B) Quantification of anti-callose immunostaining in WT, *mctp3/4* and *mctp3/4/6*.

(C-D) *sac7-1* mutant. (C) DRONPA-s diffusion assay in WT and *sac7-1* meristematic epidermal cells. (i) Schema of phosphoinositide metabolism depicting the role of SAC7 as PI4P phosphatase. (ii) Representative images of DRONPA-s diffusion. (iii) Normalized DRONPA-s fluorescence over time. Line indicates mean. Bars show SEM. (iv) Percentage of DRONPA-s normalized fluorescence in the N±1 cells at 120 seconds post activation from (iii) Statistical analysis was done using Student t-test. (D) Quantification of anti-callose immunostaining in WT and *sac7-1*. Statistical analysis was done using Student t-test

562 (E-F) *sac7-1* mutant, BRZ treatment; DMSO or 1 µM BRZ for 24 h (A) DRONPA-s mobility assay in treated WT
563 and *sac7-1*. (i) Representative images of DRONPA-s diffusion. (ii) Normalized DRONPA-s fluorescence over time.
564 Line show mean. Error bars show SEM. (iii) Percentage of DRONPA-s normalized fluorescence in the N±1 cells at
565 120 s post activation from (ii). (F) Quantification of anti-callose immunostaining in treated WT and *sac7-1*.
566 When not differently stated, statistical analysis was done using ANOVA followed by Tukey's test. Lines indicate
567 median. Error bars indicate 95% CI. Different letters indicate $p<0.05$. A minimum of 5 plants per genotype, per
568 condition, per experiment were used. Experiment were repeated 3 times and data were pooled together.
569

570 **SAC7 PI4P phosphatase is a cortical ER protein that closely associates with plasmodesmata**
571 **in a cell type specific manner**
572

573 Our data suggest that graded PI4P levels have the capacity to modulate plasmodesmata
574 connectivity. We next addressed the mechanistic bases of this regulation and whether variations
575 of PI4P levels are relevant to regulate plasmodesmata connectivity in a wild-type situation. To this
576 end, we focused on the SAC7 enzyme, because i) the *sac7* mutant showed impaired
577 plasmodesmata connectivity and ii) we found SAC7 in our plasmodesmata proteome (Brault et al.,
578 2019).
579 To analyze SAC7 expression pattern and subcellular localization, we transformed the *sac7* mutant
580 with p*SAC7::mCitrine-SAC7* and p*SAC7::2xmCherry-SAC7* constructs. Both fusion proteins
581 complemented the short root hair phenotype of the *sac7* mutant showing that they were functional
582 (**Figure S9 A-B**). Looking at SAC7 localization in root, we immediately noticed a distinct tissue-
583 specific expression pattern, with SAC7 being predominantly expressed in the root hair cell file
584 (trichoblast) while being present at much lower levels in non-root hair cells (atrichoblast) (**Figure**
585 **6A-B**). To confirm the strong expression of SAC7 in trichoblast cells, we crossed the
586 *pSAC7::2xmCherry-SAC7* line with the *EXP7 SAND* reporter line, which is exclusively expressed
587 in trichoblast cells (Marquès-Bueno et al., 2016). Colocalization revealed that 2xmCherry-SAC7
588 was indeed preferentially expressed in trichoblast, and was present in the meristem before the
589 bulging and elongation of root hairs (**Figure 6B**).
590 We next analyzed the subcellular localization of *pSAC7::2xmCherry-SAC7.* The protein
591 accumulated at the tip of growing root hairs, as previously reported (**Figure S9C**) (Thole et al.,
592 2008). We also noticed that SAC7 localized in reticulated structures in root hairs that reminded us
593 of the ER membranes. Because SAC7 was localized in the ER in BY–2 cells, and its yeast and
594 animal orthologs, Sac1p/SAC1, are ER-resident proteins (Dubois and Jaillais, 2021), we explored
595 whether SAC7 could locate in this compartment in Arabidopsis. To this end, we analyzed the
596 localization of SAC7 in cotyledon epidermis, a cell type with a stereotypical reticulated ER, and
597 confirmed that mCitrine-SAC7 colocalized with the ER marker DDRGK Domain-containing
598 protein 1-mCherry (DDRGK1-mCherry) in this cell type (**Figure S9D**) (Stephani et al., 2020). In
599 the root meristem, SAC7 also displayed an ER-localisation pattern while exhibiting a pronounced
600 enrichment at the apico-basal cortical region of the cell (**Figure 6C**).
601 To gain further insights into this unique localization pattern, we compared the localization of SAC7
602 (mCitrine-SAC7 and 2xmCherry-SAC7) with various ER markers, including the cortical ER
603 marker SYT1-GFP, the bulk ER membrane proteins DDRGK1-mCherry and Cinnamate-4-

604 hydroxylase-GFP (C4H-GFP) and the ER luminal marker RFP-HDEL (**Figure 6D**). To quantify
605 the cortical enrichment of SAC7, we used the Apico-basal vs Intracellular Fluorescence ratio
606 (APIFR) across all ER proteins (**Figure 6E**). SYT1, an ER-PM tether (Pérez-Sancho et al., 2015b),
607 exhibited an enrichment in the cortical ER similar to SAC7 (**Figure 6D-E**). However, unlike
608 SAC7, SYT1 also accumulated at the lateral sides of atrichoblast cells (**Figure 6D**). All the other
609 ER proteins displayed a more uniform distribution without significant enrichment at the cortical
610 ER and a prominent labeling of the perinuclear ER (**Figure 6D-E**). Together, these results
611 highlight a unique polar localization of SAC7 in the apical-basal cortical ER membranes.
612 As plasmodesmata were previously reported to be enriched at the apico-basal cell-cell interface as
613 opposed to lateral sides in Arabidopsis root epidermis (Zhu et al., 1998). We therefore checked
614 SAC7 association with MCTP4. Using high resolution airyscan microscopy, we colocalized
615 2xmCherry-SAC7 with GFP-MCTP4 both expressed under their native promoters. We noticed
616 that 2xmCherry-SAC7 accumulated adjacent to GFP-MCTP4-labeled plasmodesmata (**Figure**
617 **6F**). Thus, SAC7 is an ER protein, enriched in the apico-basal cortical ER of trichoblast cells, in
618 close association with plasmodesmata. Together, these data suggest that the SAC7 PI4P
619 phosphatase have the potential to regulate PI4P levels at or near plasmodesmata.
620

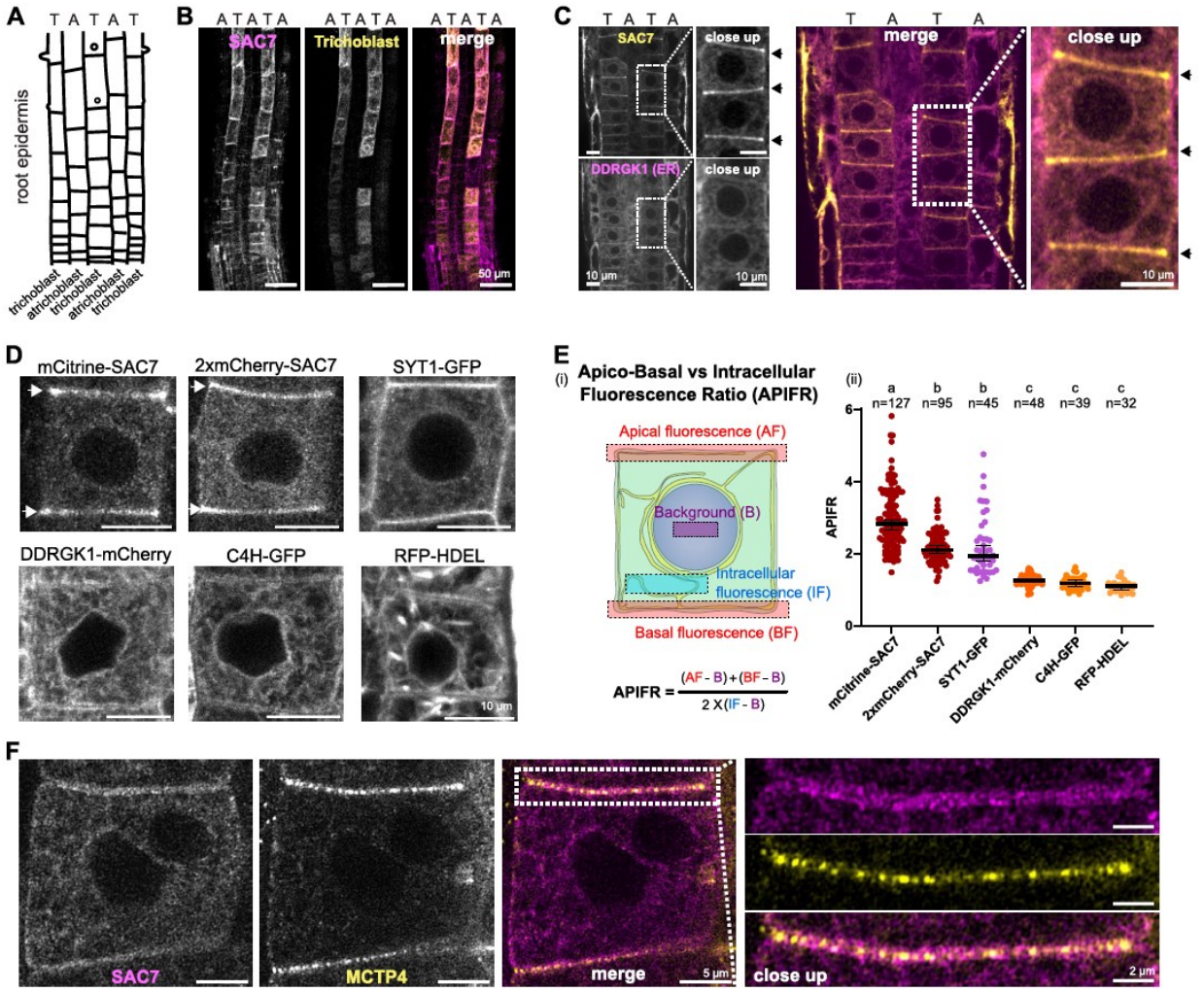

Figure 6: SAC7 is preferentially expressed in trichoblast cells and is polarly localized in the ER in proximity to MCTPs

(A) Schematic representation of the root epidermis showing the alternate pattern of root hair cells (trichoblasts, T) and non-root hair cells (atrichoblast, A).

(B) Confocal micrographs showing the overlapping expression of *pSAC7::2xmCherry-SAC7* with *pEXP7::4xYFP* (trichoblast marker) in root-tip epidermis.

(C) Confocal images showing the colocalization of *pSAC7::mCitrine-SAC7* (yellow) and *pUBQ10::DDRGK1-mCherry* (bulk ER marker, magenta) in the root meristem. Note the alternate accumulation in trichoblasts (T) but not in atrichoblasts (A).

(D) Confocal images of the indicated ER-localized proteins in root meristematic cells. White arrows point toward apico-basal accumulation of SAC7 protein.

(E) (i) Calculation of apical-basal vs intracellular fluorescent ratio (APIFR). (ii) Quantification APIFR of the proteins shown in (D). Statistical analysis was done with ANOVA followed by Tukey's test. Lines indicate median. Error bars indicate 95% CI.

(F) Confocal airyscan micrographs of roots coexpressing *pSAC7::2xmCherry-SAC7* (magenta) and *pMCTP4::MCTP4-GFP* (yellow) in root-tip epidermis cells, with a zoom of the apical-basal cell-cell interface.

642 **SAC7 is a cell-type specific regulator of MCTP localization and plasmodesmata connectivity**

643 Our data indicate that PI4P levels regulate MCTP4 interaction with the PM and cell-cell
644 connectivity. SAC7 is a PI4P phosphatase that localizes in proximity to MCTP4, and is
645 differentially expressed in trichoblast/atrichoblast cells with high expression in the trichoblast cells
646 (low PI4P) and low expression in the atrichoblast cells (high PI4P). We thus hypothesized that
647 SAC7 might function as a negative regulator of MCTP and cell-to-cell connectivity. We first
648 analyzed whether the localization of GFP-MCTP4 expressed under its native promoter differed
649 between trichoblast and atrichoblast cells in wild-type plants. To this end, we counter-stained the
650 cell wall using propidium iodine (PI) and automatically segmented the cell's contour. We then
651 quantified the GFP-MCTP4 signal at cell-cell junctions in trichoblast and atrichoblast cells (see
652 **Figure 6E**). Using this pipeline, we found that MCTP4 accumulated at significant higher levels at
653 the apical-basal interface in the atrichoblast cell files (which display low SAC7 expression levels)
654 compared to trichoblast cells (which display high SAC7 expression levels) (**Figure 7A**).

655 We next investigated how the differential localization of GFP-MCTP4 in trichoblast and
656 atrichoblast cells affects cell-to-cell connectivity within these two cell files in wild-type plants.
657 For that, we specifically quantified the dynamics of DRONPA-s diffusion in each cell file. We
658 found that DRONPA-s diffused more rapidly in trichoblast than in atrichoblast cells, correlating
659 with the high expression of SAC7 in this cell type and lower MCTP4 accumulation (**Figure 7B**).
660 We then wondered if eliminating SAC7's differential cell type expression would impact MCTP4
661 localization and thereby cell-cell connectivity. To this end, we expressed both GFP-MCTP4 (under
662 its native promoter) and cytosolic DRONPA-s in *sac7-1* mutant background. We observed a strong
663 increase of GFP-MCTP4 signal at the apico-basal walls of trichoblast cells in *sac7*. We also found
664 a slight, but significant, increase of GFP-MCTP4 in *sac7* atrichoblast cells compared to wild-type,
665 likely due to the weaker expression of SAC7 in this cell type. These changes in MCTP4
666 localization correlated with a modification of cell-cell molecular flow, which was diminished in
667 the *sac7-1* mutant compared to the wild-type with the most significant impact in the trichoblast
668 cell file (**Figure 7B**).

669 We then asked how low PI4P levels would impact plasmodesmata structure. To investigate this,
670 we returned to electron tomography on high pressure frozen freeze substituted root samples.
671 Because it is difficult to unambiguously distinguish between trichoblast and atrichoblast cells
672 without cell type markers, we generated SAC7 over-expressing lines (p*UBQ10::2XmCherry-Myc-*
673 *SAC7*). We screened through the apico-basal walls in the epidermis division zone (as for **Figure1**
674 **A**). We found that plasmodesmata in SAC7 overexpressing lines presented clear and frequent ER-
675 PM detachment events (~96 % plasmodesmata; n=23) (**Figure7C; Movie S12)** similar to *mctp*
676 triple mutants (**Figure 1C**).

677 Our results suggest that the graded expression of SAC7 impacts MCTP4 localization in a cell type
678 dependent manner, thereby directly regulating plasmodesmata connectivity. As a result, at the root
679 tip, two cell types of the wild-type epidermis show different degrees of cell-to-cell molecular

680 diffusion. Trichoblast and atrichoblast cells have different elongation rates, physiological status,
681 interactions with the underlying cortex and overall have specific functions in root biology.
682 Although the physiological impact of the differential connectivity of these two cell files remains
683 to be determined, our data serve as a proof-of-concept that an ER/PM crosstalk, via the
684 developmental modulation of PI4P/MCTP interactions, can regulate plasmodesmata connectivity.

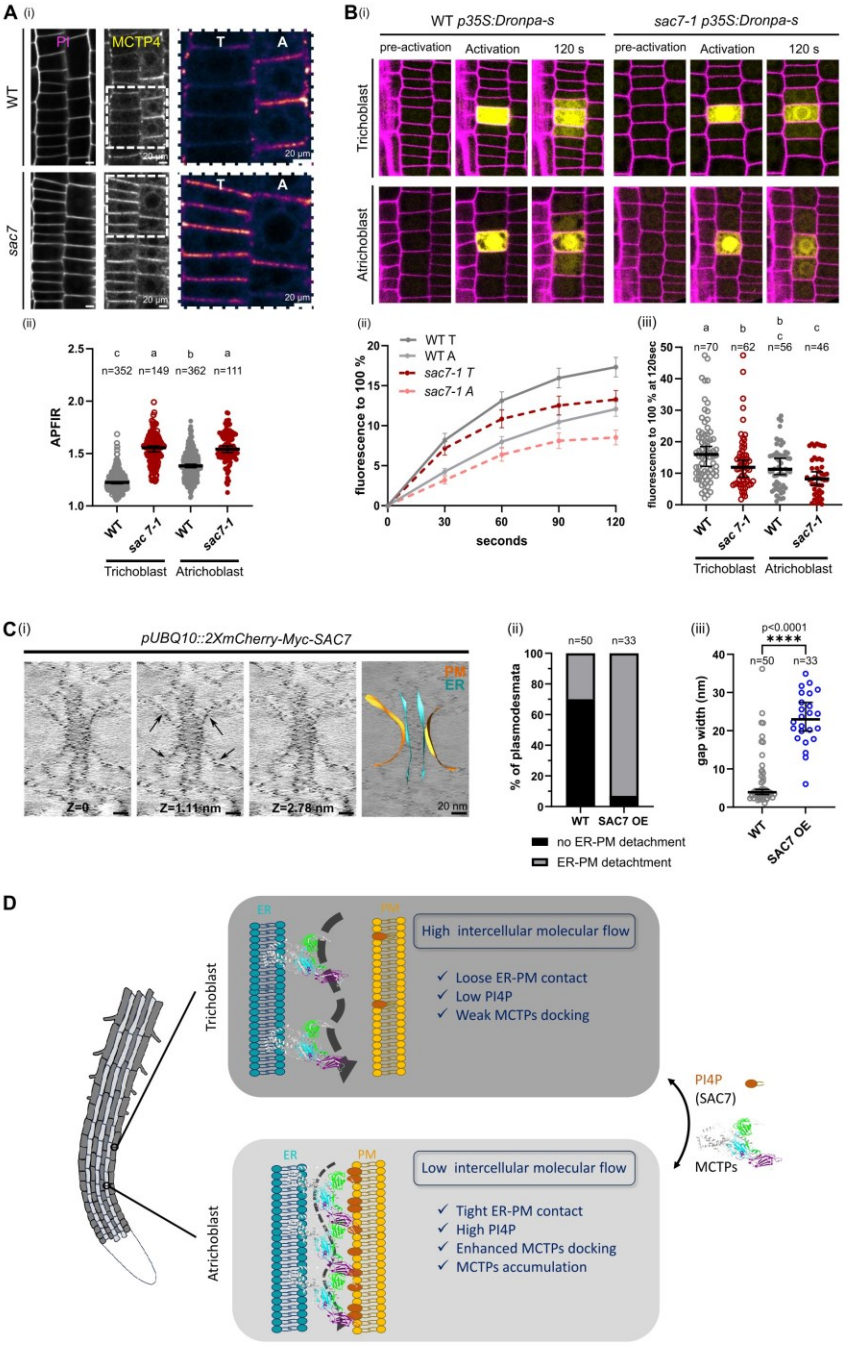

Figure 7: SAC7 regulates MCTP localization and cell-to-cell diffusion in a cell type-specific manner
(A) APIFR of *pMCTP4::MCTP4-GFP* in WT or *sac7-1* trichoblast (T) and atrichoblast (A) cells. (i) Representative confocal images. PI is used to visualized cell peripheries. (ii) APIFR quantification. Statistical analysis was done with ANOVA followed by Tukey's test. Lines indicate median. Error bars indicate 95% CI.
(B) DRONPA-s diffusion assay in WT and *sac7-1* trichoblast and atrichoblast meristematic cells. (i) Representative images of DRONPA-s diffusion. (ii) Normalized DRONPA-s fluorescence over time. Lines indicate mean. Bars show

692 SEM. (iii) Percentage of DRONPA-s normalized fluorescence in the N±1 cells at 120 seconds post activation from
693 (iii). Statistical analysis was done with ANOVA followed by Tukey's test. Lines indicate median. Error bars indicate
694 95% CI.
695 (C) (i) Individual tomographic slices and segmented 3D reconstruction of plasmodesmata in WT and *sac7-1*. Arrows
696 pointing to ER-PM detachment. (ii) Contingency plot of the percentage of plasmodesmata showing ER-PM
697 detachment. (iii) Quantification of the distance between ER and PM in WT and *sac7-1* plasmodesmata at the point
698 where the gap is the widest. Lines show median. Error bars show 95 % CI. Please, note that WT values in graphs (ii)
699 and (iii) are the same as in Fig 1C (ii) and (iii).
700 (D) Cell-type dependent dynamic regulation of plasmodesmata MCS and its impact on molecular traffic
701

702 **DISCUSSION**

703 Our results uncover two important findings. Firstly, we reveal that while MCS are typically
704 linked to inter-organellar communication in eukaryotes, they can also operate at cell-cell interface
705 to govern inter-cellular communication. Plasmodesmata bridges are prevalent across the Plantae
706 kingdom. Here, we show that they function as unconventional tubular ER-PM MCS regulating
707 direct molecular exchange between neighboring cells. Similar to other MCS, the regulation of
708 membrane contacts at plasmodesmata involves a complex molecular partnership consisting of
709 phosphoinositides and protein tethers. However, in contrast to the typical MCS, which primarily
710 govern direct molecular exchange between organelles, plasmodesmata MCS serve to control the
711 flow of molecules between adjacent cells (**Figure 7D**). To our knowledge, this marks the first
712 discovery of the functional involvement of MCS in direct intercellular exchange and hints at a new
713 conceptual framework. Recent findings support the notion that MCS may also function in cell-cell
714 communication in animals. A recent preprint reports two ER-PM MCS-associated proteins,
715 TMEM24 and C2CD2, to be involved in cell-cell contact interaction in neurons (Johnson et al.,
716 2023), although experimental support for effective communication is still lacking. Likewise,
717 Bharathan et al. described close contact between the ER and desmosomal intercellular junctions
718 (Bharathan et al., 2023). This work has sparked inquiries into whether an integrated ER-keratin-
719 desmosome contact zone could facilitate the transmission of ER stress signals between cells. Our
720 study brings this concept one step further and demonstrates the functional involvement of
721 multicellular eucaryotic MCS in direct intercellular exchanges. The second important outcome of
722 this study is to propose a novel regulatory mechanism for cell-cell trafficking underscoring the
723 significance of MCS. Right now, the textbook model depicts callose as the master regulator of
724 plasmodesmata. Unquestionably, numerous studies report the involvement of callose in opening
725 or closing plasmodesmata in a wide range of developmental and physiological responses. The
726 prevailing concept behind callose action is that callose build-up would create pressure on the PM,
727 causing it to push against the ER, therefore obstructing cellular traffic by reducing the size of the
728 cytoplasmic sleeve. However, recent research in the field suggests that callose actually functions
729 as a plasticizer, enhancing wall flexibility, rather than forming a rigid donut-shaped structure that
730 presses against the PM (Abou-Saleh et al., 2018). Moreover, extreme proximity between the ER
731 and the PM, which can be as little as 3-4 nm (Nicolas et al., 2017a), is likely to require membrane
732 bridging-complexes to induce and to stabilize the contact. This work suggests that without the
733 molecular machinery acting at the ER-PM interface (*i.e.* PI4P and MCTP tethers) dynamic

734 regulation of plasmodesmata is compromised even if callose regulation is still functional.
735 Collectively our data indicate that MCTP/PI4P regulate plasmodesmata opening and closing,
736 largely independent of callose levels. This finding introduces a new perspective on how
737 intercellular molecular flow is regulated in plants, and opens the door to a more intricate regulatory
738 mechanism than previously thought. How could MCTP/PI4P dynamically regulate molecular flow
739 across plasmodesmata MCS? The most straightforward hypothesis is by modulating the ER-PM
740 gap (**Figure 7D**). Theoretical models suggest that changes in plasmodesmata structure directly
741 affect the rate of molecular flow through these channels (Deinum et al., 2019; Ostermeyer et al.,
742 2022). This is notably influenced by the internal geometry and size of the cytoplasmic sleeve
743 (defined as the space between the two membranes), which determines the resistance to diffusion
744 or convective flow. The overexpression of SAC7 PI4P phosphatase leads to increased ER-PM
745 detachment events within plasmodesmata. The MCTP family comprises 16 members in
746 Arabidopsis, and the deletion of three members, specifically MCTP3, MCTP4, and MCTP6, leads
747 to a noticeable alteration in ER-PM tethering within plasmodesmata. This structural modification
748 is associated with an increase in the global molecular flow between adjacent cells. This rise in cell-
749 cell trafficking occurs in a context where loss-of-function mutants for *mctp3/mctp4* and
750 *mctp3/mctp4/mctp6* exhibit a significant reduction of approximately 30% to nearly 50% in the
751 number of plasmodesmata in the root meristem (Li et al., 2023). This suggests that the transport
752 capacity of a single plasmodesma is considerably greater in *mctp* mutant background compared to
753 wild-type. What are the underlying molecular mechanisms responsible for regulating the ER-PM
754 gap? Our data indicate that MCTPs operate in coordination with the anionic lipid PI4P. We show
755 that MCTP4 establishes a direct interaction with PI4P through its C2 domains as indicated by
756 liposome binding assays and molecular dynamics. Furthermore, molecular dynamics simulations
757 suggest that the levels of PI4P directly influence MCTP's attachment to the PM. This model is
758 corroborated by the experimental finding that when PI4P production is up- or down-regulated,
759 cell-cell transport is either hindered or facilitated. PI4P is a signaling lipid, whose level and
760 subcellular accumulation are highly regulated during development and environmental interactions
761 (Noack and Jaillais, 2020). Here, we showed that the PI4P phosphatase SAC7 regulates MCTP
762 localization and plasmodesmata connectivity in a tissue dependent manner. This serves as a proof-
763 of-concept that graded PI4P levels in a wild-type context can impact cell-cell connectivity in
764 different cell types. The SAC7-dependent regulation of MCTP localization that we observed at the
765 developmental scale can be considered a relatively slow response that is established during tissue
766 differentiation. In this scenario, PI4P binding sites inside plasmodesmata are likely limiting factors
767 for MCTP docking and ultimately will determine the overall accumulation of MCTP at cell-cell
768 interfaces. However, PI4P regulation may also occur on a shorter timescale, within minutes or
769 even seconds (Marković and Jaillais, 2022). This is notably the case during certain biotic or abiotic
770 stresses. It is also possible that some MCTP C2 domains show increased PI4P-binding upon Ca^{2+}
771 binding (Rizo and Su, 1998; Giordano et al., 2013; Yu et al., 2016). In such a scenario, PI4P and
772 Ca^{2+} variations may regulate plasmodesmata conductance very rapidly. However, this may not
773 directly translate in changes in MCTP levels within plasmodesmata. It is possible that changes in

774 PI4P concentrations might induce conditional docking of MCTPs to the PM, thereby opening or
775 closing the cytoplasmic sleeve on demand. Such scenarios have been observed in the context of
776 other MCS. For example, in human cells, the amount of PI4P at the Golgi determines the
777 conditional establishment of ER/Golgi contacts and can even generate traveling waves of MCS
778 between the two organelles (Mesmin et al., 2013; Mesmin et al., 2017). Interestingly, in this
779 example, membrane contact establishment is regulated by a PI4P phosphatase called Sac1, which
780 is orthologous to the Arabidopsis SAC7 enzyme (Dubois and Jaillais, 2021). In addition to
781 conditional docking, molecular dynamics suggest that MCTP4 C2 domains may interact with the
782 PM and PI4P in different conformations (Bian et al., 2018). Whether such conformational changes
783 exist in vivo remains to be determined but this hypothesis represents an attractive model to regulate
784 cytoplasmic diffusion on a short time scale.

785 Altogether, our study shows that ER/PM tethering not only maintains plasmodesmata structure but
786 it also suggests that the ER-PM junction can be dynamically regulated in physiological contexts
787 to regulate the connectivity of plant cells within their tissue.

788 **Limitation of the study**

789 A limitation of our work lies in the reliance on loss-of-function *mctp* alleles. The
790 *mctp3/mctp4/mctp6* loss-of-function mutant exhibits structural defects with looser ER-PM
791 contacts, indicating that MCTP tethers not only act as regulatory elements but also as structural
792 elements. One possibility is that callose may not effectively block plasmodesmata due to a
793 significant disruption in plasmodesmata structure in the *mctp* mutant lines. Moreover, we cannot
794 exclude that callose interaction with the PM or other wall-polymer is affected in *mctp* mutant
795 background modifying its action. While we do not expect MCTPs to affect extracellular wall
796 polymers or wall properties directly, we cannot rule out indirect effects. Nevertheless, our data in
797 the *sac7* mutant suggest that increased PI4P levels stabilize MCTP within plasmodesmata and
798 reduces cell-to-cell cytoplasmic diffusion even when callose deposition is almost completely
799 inhibited (i.e. after BRZ treatment). While we still do not fully understand the functional and
800 structural relationship between callose deposition and ER/PM tethering within plasmodesmata,
801 our results strongly imply that MCTP/PI4P interaction can close plasmodesmata in the absence of
802 callose.

803 In this study, we focused on the function of PI4P in the regulation of MCTP localization and
804 plasmodesmata activity. However, PI4P is not the only signaling lipid within the PM, which also
805 includes phosphatidic acid, phosphatidylserine and PI(4,5)P_2 (Platre et al., 2018). Because each
806 MCTP protein has multiple C2 domains, which all have the potential to bind to one or several
807 anionic lipids, we need to be cautious and acknowledge that PI4P is likely not the only lipid
808 regulator at plasmodesmata. In fact, we found both PI4P and PI(4,5)P_2 in our purified
809 plasmodesmata fraction. It is possible that each MCTP protein will have specific lipid preferences,
810 thereby regulating ER/PM contact in a differential manner according to the tissue analyzed and/or

811 to environmental stresses. In addition, the interaction between MCTP C2 domains and different
812 anionic lipid species may also be modulated by calcium. Altogether, we believe that MCTP/lipid
813 interactions have immense regulatory potential to fine tune plasmodesmata connectivity across a
814 broad range of time scales and with exquisite spatial and temporal specificity.

815

Acknowledgments: We would like to thank Paulo Telles de Souza for sharing Martini3 coarse grain parameter for sitosterol**.** Fabrice Cordelières for live-imaging data display. Jérome Hénin for assistance with colvars protocol. Christel Poujol, Jeremie Teillon and Sebastien Marais for assistance with SP8-STED-FLIM and SP5-2P. We would also like to thank Alexandre Martinière, Yohann Boutté, and Sébastien Mongrand for reading and commenting on the article. Light and electron imaging were done at the Bordeaux Imaging Center, member of the national infrastructure France-BioImaging supported by the French National Research Agency (ANR-10-INBS-04) or at the RDP lab (ENS Lyon, France). We acknowledge the contribution of the SFR Biosciences (UMS3444/CNRS, US8/Inserm, ENS de Lyon, UCBL) E. Chatre, and J. Brocard at LBIPLATIM-MICROSCOPY for assistance with imaging, and Claire Lionnet for assistance with imaging at the RDP. The lipid analysis was done at the Bordeaux Metabolome platform for lipid analysis (https://www.biomemb.cnrs.fr/en/lipidomic-plateform/) supported by Bordeaux Metabolome Facility-MetaboHUB (grant no. ANR–11–INBS–0010 to LF). We thank Yohann Boutté for his help in anionic lipid extraction, Lothar Kalmbach for the pLOK180 plasmid gift, Yasin Dagdas for the DDRGK1-mCHERRY line and Thomas Eekhout (VIB) for the scRNA seq data mining.

Funding: This work was supported by the European Research Council (ERC) under the European Union's Horizon 2020 research and innovation program (project 772103-BRIDGING to E.M.B. and 101001097-LIPIDEV to Y.J.); the National Agency for Research (Grant ANR-18-CE13-0016 STAYING-TIGHT to E.M.B and Y.J.; ANR-21-CE13-0016-01 DIVCON to A.T. and E.M.B; ANR-18-CE13-0025-02 caLIPSO to Y.J.); the Human Frontier Science Program (project RGP0002/2020, E.M.B.); the French government in the framework of the IdEX Bordeaux University "Investments for the Future" program / GPR Bordeaux Plant Sciences (E.M.B.). Swiss National Science Foundation (project 31003A_179159 to MB. Research Foundation-Flanders grant G002121N (to E.R.) and the HORIZON-MSCA-2023-PF-01 project 101152141-BRACTION (to Y.L.).

Author contributions:

Conceptualization: J.P-S., M. S., Y.J., E.M.B

Methodology: J.P-S., M. S., G.D., M.G., S.S., G.D., L.F., F.I., J.T., A.T., Y.J., E.M.B

Validation: J.P-S., M. S., G.D., A.T., Y.J., E.M.B

Investigation: J. P-S, M.S., G.D., M.G., S.S., G.D. V.D., M.P.P., Z. P.L., H.M., A.P., Y.L., L. F., M.S.G., P. C-Q, T. S.M., F.I., V.W., M.D., L.B., P.R., V.B., L.L.L., C.C., S.C., M.Z., Y. L., M.Z.

Supervision: Y.J., E.M.B.

Funding acquisition: A.T., Y.J., E.M.B,

Writing – original draft: J.P-S, M.S., Y.J., E.M.B

Writing – review & editing: J.P-S, M.S., G.D., V.D., A.P., P. C-Q, M.P.P., J.T., E.R. M.B., Y.H., A.T., Y.J., E.M.B

Declaration of interests: The authors declare no competing interests.

Data and materials availability: All data are available in the main text or the supplementary materials

METHODS

- Plant material

Arabidopsis thaliana, accession Columbia (Col-0), (which we are referring to as wild-type-WT) and transgenic lines (all in Columbia background) were surface sterilized, vernalized at 4C during 2 days and grown vertically on solid half-strength Murashige and Skoog media supplemented with vitamins (2.15 g/L), MES (0.5 g/L), sucrose (10 g/L) and plant agar (7 g/L), pH 5.7 for 6 days at 22°C in a 16-h light/8-h dark cycle with 70% relative humidity and a light intensity of 200 µmol x m^{-2} x s^{-1} prior to use. Recently harvested, synchronized seeds were used for all phenotypical analysis. *Nicotiana benthamiana* plants were grown in an insect proof greenhouse with 18/25°C night/day.

The following lines were previously published and characterized *rhd4-1/sac7-1* (EMS) and *rhd4-3/sac7-3* (SALK_079231) (Thole et al., 2008), *EXP7pro::4xYFP* (Marquès-Bueno et al., 2016), DDRGK1-mCHERRY (Stephani et al., 2020) , *SYT1pro:SYT1-GFP* (Pérez-Sancho et al., 2015b), C4H-GFP (Lee et al., 2019b), RFP-HDEL (Pain et al., 2019), *mctp3-2/mctp4-1* mutant and *MCTP4pro::*GFP-MCTP4 (Brault et al., 2019), *35Spro::DRONPA-s* (Gerlitz et al., 2018)

- Cell culture

Arabidopsis (*Landsberg erecta*) culture cells were cultivated as described in Bayer et al. (Bayer et al., 2004) under constant light (20 µE/m/s) at 22°C. Cells were used for plasmodesmata extraction at 7 days old.

- Cloning and plasmid construction

In this study, the constructs employed were derived from Col-0 cDNA/genomic DNA, or were synthesized. The promoter sequences were integrated into pDONR-p4RP1, while the genes and fluorescent tags were integrated into either pDONR221 or pDONR-P2RP3, utilizing the MultiSite-Gateway cloning system. For the development of an inducible genome editing vector, plasmids containing the inducible RPS5A promoter, codon-optimized and RFP-tagged Cas9, along with two sgRNAs, were assembled using the Gateway system. The assembly of all constructs was carried out through multi-Gateway reactions, wherein three segments were cloned into the destination vector, pLOK180, which express a red seed-coat selection marker (a gift from L. Kalmbach).

887 The expression vectors were introduced into *Agrobacterium tumefaciens* strain GVG3101, which
888 was then used to transform Arabidopsis Col-0 or *mctp* mutants (as indicated in the figure legends)
889 through the floral dip method, as previously described (Clough and Bent, 1998). Transformed seeds
890 were selected based on the presence of either red seed coat or BASTA resistance, depending on
891 the selection marker used. We employed a similar selection scheme as described in (Lebecq et al.,
892 2022), which ensures that for each transgenic lines selected, several independent transformants,
893 with a single insertion, show similar results. Briefly, between 20 and 24 independent T1 (Basta or
894 Green/Red seed coat) were selected and propagated. In T2, all lines were screened using confocal
895 microscopy for fluorescence signal and localization. Between 3 and 5 independent lines with a
896 mono-insertion and showing a consistent, representative expression level and localization were
897 selected and grown to the next generation. Each selected line was reanalyzed in T3 by confocal
898 microscopy to confirm the results obtained in T2 and to select homozygous plants. At this stage,
899 we selected one representative line for in-depth analysis of the localization.

900 Cloning of SAC7-related material: The SAC7 promoter (Sac7pro, 1963bp upstream of
901 AT3G51460 START codon) was amplified from Col-0 DNA and inserted in the pENTR-5'-TOPO
902 Gateway vector using TOPO cloning (Invitrogen™). The coding sequence (CDS) of SAC7 (ATG
903 to STOP codon) was amplified by PCR from Col-0 cDNA and recombined by BP reaction into
904 pDONR-P2R-P3. The mCITRINE/pDONR 221, and 2xmCHERRY-1xmyc/pDONR P221 and
905 UBQ10pro/pDONRP4RP1 were published before (Jaillais et al., 2011; Simon et al., 2014). The
906 LR clonase-based three-fragment recombination system (Invitrogen®) was used to produce the
907 pSAC7::mCitrine-SAC7 into pLOK180_pR7m34g (a gift from L. Kalmbach, red seed selection)
908 and pSAC7::2xmCherry-Myc-SAC7; pUBQ10::2xmCHERRY-Myc-SAC7into
909 pLOK292_pFG7m34G (a gift from L. Kalmbach, green seed selection).

910 To generate the inducible *PDR9xve::cals3m,* a 2kb DNA fragment corresponding to *PDR9*
911 promoter, active in the epidermis (Robe et al., 2021) was cloned into p1R4-ML:XVE (Siligato et
912 al., 2016) and subsequently assembled by multi-site gateway technology into the destination
913 plasmid pFG7m34GW (Kalmbach et al., 2023) together with *casl3m* (Vaténet al., 2011) in
914 pDONR221 and the terminator tNOS in pDONRP2R-P3 (Karimi et al., 20007)

915 - Transient expression in *Nicotiana benthamiana*

916 The abaxial side of leaves of 3- to 4-week-old *Nicotiana benthamiana* plants were pressure-
917 infiltrated with GV3101 agrobacterium strains carrying the different constructs. Prior to
918 infiltration, the agrobacterium cultures were grown overnight in Luria and Bertani medium
919 supplemented with rifampicin (50 mg/mL), gentamycin (25 mg/mL), and the construct-specific
920 antibiotic at 28°C. Subsequently, the cultures were diluted to 1/10 in the same growing medium
921 (without Rifampicin) and further cultivated until the optical density at 600 nm (OD600) reached
922 approximately 0.6-0.8. The bacterial cells were then collected through centrifugation at 3000g for
923 5 min, followed by resuspension in agroinfiltration solution (10 mM MES, pH 5.6, 10 mM MgCl2,
924 and 1 mM acetosyringone) and incubated for 2h at room temperature and in the dark. For
925 infiltration of individual constructs, a final OD600 of 0.3 was used. For co-infiltration of two

926 constructs, and OD600 of 0.2 each was used. Additionally, the ectopic silencing suppressor p19
927 was co-infiltrated in all the cases at an OD600 of 0.05. Post-infiltration, plants were kept in the
928 same growing conditions as before for 2 more days; then leaf-discs were collected from the N.
929 benthamiana leaves and subjected to imaging at room temperature.

930 - Lattice light sheet

931 The Lattice Light Sheet Microscope (LLSM) was built according to the technical information
932 provided by the group of E. Betzig at Janelia Research Campus, Howard Hughes Medical Institute
933 (HHMI), USA. The lattice light sheet was focused by a custom excitation objective 28.6× 0.66
934 numerical aperture 3.74-mm (Special Optics). Fluorescence was collected with a CFI Apo LWD
935 1.1 numerical aperture 25× 2.0-mm detection objective (Nikon) and imaged on a scientific
936 complementary metal-oxide semiconductor (sCMOS) ORCA-Flash4.0 V2 camera (Hamamatsu).
937 The annular mask minimum and maximum numerical apertures were 0.35 and 0.4, respectively,
938 thus creating a light sheet with a uniform thickness over length > 30µm. All images were acquired
939 in dithered square lattice mode. We characterized the LLSM optical resolution at l_{em}=510nm using
940 170nm diameter beads. We found 275 +/- 5 nm and 690 +/- 10 nm, laterally and axially
941 respectively. Images were acquired at ~10 to 20 µm below the surface of the root. Fast sample
942 translation with a piezo stage was used to acquire Z stacks with a step of 300 nm. Typical laser
943 power incident on the excitation objective is ~ 0.4mW. The raw data are 3D deconvolved with an
944 open-source Richardson Lucy (RL) algorithm (https://github.com/dmilkie/cudaDecon) using an
945 experimental PSF. The RL software is bundled into LLSpy, a python LLSM data processing and
946 visualization toolbox (https://github.com/tlambert03/LLSpy). Deconvolution runs on a CUDA
947 compatible GPU graphics card. A 3x3 median filter (noisy pixel removal) followed by background
948 subtraction is applied before RL deconvolution with 10 iterations.

949 - Laser Scanning Confocal Microscopy

950 In the conducted live-imaging experiments, a Zeiss LSM 880 confocal microscope equipped with
951 40x and 63x oil-immersion objectives, as well as 40x water immersion objectives, was employed.
952 The microscope was controlled using ZEN Black 2011 software. The experiments were carried
953 out at a controlled temperature ranging from 22 to 24 C.

954 To detect GFP in the confocal mode, a filter with an excitation (Ex) wavelength of 488 nm and an
955 emission (Em) range of 505-550 nm was utilized. For the detection of tagRFP or propidium iodide
956 (PI) fluorescence, a filter with an Ex wavelength of 556 nm and an Em range of 570-625 nm was
957 employed. To detect YFP fluorescence, a filter with an excitation (Ex) wavelength of 514 nm and
958 an emission (Em) range of 520-570 nm was utilized when imaging YFP alone. When YFP was
959 imaged together with a red reporter, we used the settings already described for GFP.

960 For Airyscan imaging, GFP or YFP fluorescence was detected using an excitation (EX)
961 wavelength of 488 nm and an emission bandpass (Em BP) range of 420-480 nm in combination

962 with 495-550 nm. On the other hand, for the detection of PI an excitation (EX) wavelength of 488
963 nm and an emission (Em) range of 620-700 nm in combination with a long pass (LP) filter at 645
964 nm were used. For callose imaging, atto550 excitation was done with 561 nm power excitation
965 and fluorescence collected between 566 and 700 nm. Callose deposition at plasmodesmata was
966 quantified with Fiji software and signal from the forming cell plae was excluded as indicated in
967 Figure 3. Calcofluor aquisition was done by 405nm excitation and collected at 410-480nm. For
968 SAC7/MCTP colocalization (Figure 6F), Airyscan imaging was conducted on 7-day-old roots
969 using an inverted LSM 980 Axio Observer Z1/7 (Carl Zeiss group, http://www.zeiss.com/) equiped
970 with an AiryScan 2 module, GaAsP-PMT detectors and a C Plan-Apochromat 40X objective
971 (numerical aperture 1.3, oil immersion).

972 To prevent signal cross-talk, image acquisition occurred by frame when two colors were imaged
973 simultaneously.

974 - Spinning Disk Microscopy:

975 Spinning disk microscopy was used in Figure 6A-D and 7A. Observations of roots of 7-day-old
976 seedlings were conducted using a Zeiss microscope (AxioObserver Z1, Carl Zeiss Group,
977 http://www.zeiss.com/) equipped with a spinning disk module (CSU-W1-T3, Yokogawa,
978 www.yokogawa.com) and a Prime 95B camera (Photometrics, https://www.photometrics.com/).
979 We used a 40x objective (Plan-Apochromat, numerical aperture 1.1, water immersion) in Figure
980 7A or a 63x objective in Figure 6A-D (Plan-Apochromat, numerical aperture 1.4, oil immersion).
981 Green Fluorescent Protein (GFP) was excited with a 488 nm laser (150mW), and the ensuing
982 fluorescence emission was filtered via a 525/50 nm BrightLine® single-band bandpass filter
983 (Semrock, http://www.semrock.com/). The mCITRINE marker was excited with a 515nm laser
984 (60mW), and the resulting fluorescence emission was directed through a 578/105 nm BrightLine®
985 single-band bandpass filter (Semrock, http://www.semrock.com/). For mCHERRY or PI labeling,
986 an excitation laser at 561nm (80mW) was applied, and the fluorescence emission was filtered using
987 a 609/54 nm BrightLine® single-band bandpass filter (Semrock, http://www.semrock.com/).

988 - Cryofixation and freeze -substitution

989 Five-day old seedlings of WT, *mctp3/4* and *mctp3/4/6* were grown vertically MS ½. Roots were
990 taken and cryofixed in 20% BSA filled copper platelets (100 nm deep and 1.5 mm wide) with EM
991 PACT1 high-pressure freezer (Leica). Subsequently, the root tissues were harvested and subjected
992 to cryopreservation by rapidly freezing them using a high-pressure freezer (Leica EM PACT1)
993 equipped with copper platelets (100 nm deep and 1.5 mm wide) filled with 20% bovine serum
994 albumin (BSA) solution. The cryofixed samples were then subjected to freeze-substitution within
995 an AFS2 system (Leica) maintained at -90 °C. The cryosubstitution process involved immersing
996 the samples in a cryosubstitution mixture containing 0.36% uranyl acetate in pure acetone for a
997 duration of 24 hours. Subsequently, the temperature was gradually increased at a rate of 3 °C per
998 hour until it reached -50 °C and held steady for 3 hours. To ensure thorough substitution, the

999 cryosubstitution mixture was replaced with pure acetone and later pure ethanol, with each solvent
1000 being applied for three 10-minute washes. The copper platelets were intentionally retained to
1001 prevent any potential loss of the samples. Infiltration of the specimens was carried out using a
1002 series of increasing concentrations of HM20 Lowicryl resin (Electron Microscopy Science),
1003 including 25% and 50% (1 hour each), 75% (2 hours), and finally 100% (overnight, 4 hours,
1004 48 hours, with fresh resin for each bath). Following infiltration, the samples were polymerized
1005 under ultraviolet light for 24 hours at -50 °C, after which the temperature was incrementally raised
1006 at a rate of 3 °C per hour until it reached 20 °C, where it was maintained for an additional 6 hours.

1007 - Tomography and Transmission Electron Microscopy

1008 Fixed root embedded in HM20 resin blocks were sectioned longitudinally into slices with a
1009 thickness of 80 nm using an EM UC7 ultramicrotome (Leica) These sections were then delicately
1010 positioned onto 200 mesh copper grids. Subsequent observations were conducted employing a FEI
1011 TECNAI Spirit 120 kV electron microscope. For plasmodesmata structure we acquired tomograms
1012 in 3 to 4 roots over two technical replicates.

1013 For the purposes of tomographic analysis, a protocol in accordance with the approach outlined by
1014 Nicolas et al., 2017a was employed. To facilitate image alignment during the tomography process,
1015 sections were coated with 5 nm colloidal fiducials. A series of tilt images spanning an angular
1016 range from -65° to 65° was acquired with a 1° angular increment using the FEI 3D explore
1017 tomography software. Subsequently, tomographic reconstructions were generated utilizing the
1018 eTomo software (http://bio3d.colorado.edu/imod/). Segmentation tasks were carried out
1019 employing the 3dMOD software (https://bio3d.colorado.edu/imod/doc/3dmodguide.html).

1020 - Forester Resonance Energy Transfer-Fluorescence Lifetime Imaging (FRET-FLIM)

1021 The confocal microscope used for FRET FLIM was a Leica SP8 WLL2 on an inverted stand
1022 DMI6000 (Leica Microsystems, Mannheim, Germany), using objectives HC Plan Apo CS2 40X
1023 oil NA 1.30. The confocal microscope was equipped of a pulsed white light laser 2 (WLL2) with
1024 freely tuneable excitation from 470 to 670 nm (1 nm steps) and a pulsed diode at 440 nm and also
1025 a diode laser at 405 nm.

1026 The scanning was done using either a conventional scanner (10Hz to 1800 Hz) or a resonant
1027 scanner (8000Hz). The microscope was composed of 2 internal photomultiplier tubes (PMT), 2
1028 internal hybrid detectors and 1 external PMT for transmission. For excitation of the donor
1029 *pMCTP4::e-YFP- MCTP4*, 516nm laser was used. The confocal microscope was equipped with
1030 the FALCON module for FLIM measurements. We used 5 iterations in order to acquire enough
1031 photon counts (10-4). Monoexponential fit was applied for both donor alone and donor with the
1032 acceptor (*pMCTP3::mCherryMCTP3*) and values were extracted only from the plasmodesmata
1033 signal.

1034 - Two-photon microscopy and cell diffusion assay with DRONPA-s

1035 5-day-old 35S::DRONPA-s seedlings was cultivated on ½ MS plates under long-day conditions at
1036 21 °C with 70% humidity. Subsequently, these seedlings were transferred to either DMSO or
1037 200nM Brassinolide plates for an additional 24 hours. The root tips of the seedlings were subjected
1038 to analysis using a Leica TCS SP5-Multi photon confocal microscope setup. Prior to imaging, the
1039 plants underwent a 2-minute incubation in a 1/500 propidium iodide (PI) solution in water. PI was
1040 excited at 488 nm and its emissions were detected at 620-700 nm. Leica LAS AF software was
1041 employed for the quantification of fluorescence intensities.

1042 The movement of DRONPA-s was captured as follows:

1043 1. DRONPA-s deactivation: Root tips were illuminated with 488 nm light for 45 seconds at
1044 70% of the total laser intensity using an argon laser (20mW, Leica Microsystems).
1045 2. DRONPA-s activation: Three Regions of Interest (ROIs), each corresponding to a single
1046 cell per root, were selected at the cell center to avoid activating adjacent cells. These ROIs
1047 were exposed to 5 seconds of 800 nm light using a two-photon IR (Titane-Saphir pulsating
1048 laser). The laser power used was approximately 2.6W with a 20% gain.
1049 3. DRONPA-s acquisition: Detection was conducted 2 seconds after the single cell activation
1050 and continued for 120 seconds, using a 20% 488 nm argon laser at an emission range of
1051 500-575 nm.

1052 DRONPA-s movement analysis involved measuring mean fluorescence intensities from the
1053 activated cell and the two adjacent cells using ImageJ. DRONPA movement was calculated based
1054 on the fluorescent signal transferred from the activated cell to the adjacent cells. Any X-Y drifts
1055 were corrected with the StackReg plugin. Following normalization and background subtraction,
1056 the values were converted into a percentage of the average fluorescence from the two adjacent
1057 cells. The activated cell was considered to have 100% DRONPA-s molecules activated in the ROI.
1058 A total of more than 20 roots were analyzed, with 2-3 ROIs per root.

1059 - Fluorescence Recovery After Photobleaching

1060 PI permeability assessments were made using FRAP on six day-old Arabidopsis root tips co-
1061 stained with CFDA (50µg/mL) and Propidium iodide.Roots were incubated in an aqueous CFDA
1062 solution for 5 minutes, then successively washed out in 3 water baths and mounted with propidium
1063 iodide in water for imaging FRAP experiments were conducted using a Zeiss LSM 880 confocal
1064 microscope, which was equipped with a Zeiss CPL APO x 40 oil-immersion objective (numerical
1065 aperture 1.3). To excite CFDA, a 488 nm wavelength was utilized with 100% of argon laser power,
1066 and the fluorescence emission was collected within the 505–550 nm range using a GaAsp detector.
1067 Photobleaching was performed on rectangular regions of interest (ROIs) encompassing three
1068 epidermal cells, with the exciting laser wavelengths set to 100%. The FRAP procedure involved
1069 capturing 10 pre-bleach images, followed by 15 iterations of bleaching, with a pixel dwell time of

1.31 µs. Subsequently, 90 post-bleach images were acquired. The recovery profiles were subjected to background subtraction and then double normalization through the FRAP analysis website https://easyfrap.vmnet.upatras.gr/ (Koulouras et al., 2018).

- Quantification of the Apico Basal Vs Intracellular Fluorescence Ratio (APFIR):

Two methods were used to obtain the APFIR, a "manual" approach with a draw-by-hand fluorescence extraction ROI method on Fiji (Figure 6) and an "automated" pipeline with a Fiji macro (Figure 7). In figure 6, we could not use the automated approach because the signals from the various ER markers were too different (perinuclear and diffuse vs subcortical) leading to error in the segmentation.

Fluorescence extraction:

Manual method: the intracellular fluorescence was extracted on each cells by drawing an ROI close to the nucleus to capture most of the perinuclear ER, the apico-basal fluorescence was extracted by drawing two ROI at the apical and basal membranes of each cells, the background fluorescence was extracted by drawing an ROI inside the nucleus. *Automated method*: This method requires a segmentation of all the cells, which is done with the red channel (propidium iodine staining of the root). Subsequently to segmentation, the fluorescence of interest (green channel) is extracted at different ROI automatically determined by the macro for each cells: the intracellular fluorescence (the entire fluorescence inside the cell); the apical membrane fluorescence, and the basal membrane fluorescence. The macro can be found at:

https://github.com/RDP-vbayle/SiCE_FIJI_Macro/blob/main/misc/MacroAPFIR_Perez-Sancho_et_al_221020.ijm

Calculation of the APFIR:

No background substraction is done on the ROI fluorescence values obtained via the automated method. For the fluorescence values obtained via the manual method, the values of the ROI fluorescence (apical, basal, intracellular) is subtracted by the value of the background of the same cell. For each cell, the APFIR is calculated as the mean apico-basal fluorescence divided by the intracellular fluorescence.

- Co-Immunoprecipitation in *Nicotiana benthamiana*.

The appropriate constructs were transiently expressed in Nicotiana bentamiana (see Transient expression in *Nicotiana benthamiana* section). Two plants per construct combination and two whole leaves per plant were agroinfiltrated. Using a puncher, 10 leaf-discs were collected for each leaf, so 40 leaf-discs per construct combination, and immediately frozen in liquid nitrogen (aprox 0.5 g of tissue). Frozen tissue was grinded using mortar and pestle and total proteins were extracted

1104 with 1 mL of extraction buffer (150 mM Tris-HCl, pH 7.5; 150 mM NaCl; 10 % glycerol; 10 mM
1105 EDTA, pH 8; 1mM NaF; 1 mM Na2MoO4; 10 mM DTT; 0.5 mM PMSF; 1% (v/v) P9599 protease
1106 inhibitor cocktail (Sigma); 1 % (v/v) Igepal) by incubating during 40 min at 4 C with continuous
1107 mixing in an end-over-end rocker. Samples were centrifuged for 20 min at 4C and 9,000 g.
1108 Supernatants were filtered by gravity through Poly-PrepChromatography Columns (#731-1550
1109 Bio-Rad). For each sample, 50 uL of the filtered supernatant were collected and mixed with 50 uL
1110 of Laemmli buffer (Tris-HCl pH 6.8 125 mM; 4% SDS; 20 % (v/v) glycerol; 2 % (v/v) beta-
1111 mercaptoethanol; 0.01 % bromophenol blue) for immunoblot analysis as input. The remaining
1112 filtered supernatants were mixed in a 1:1 proportion with wash buffer (extraction buffer without
1113 Igepal) to reach a final concentration of 0.5 % Igepal in the samples before adding the GFP-Trap
1114 agarose beads (as recommended by the manufacturer to avoid nonspecific binding). 15 uL of
1115 equilibrated GFP-Trap agarose beads were added to each sample and incubated during 2 h at 4 C
1116 with continuous mixing. After incubation, samples were centrifuged 30 s at 500 g to precipitate
1117 the beads Then beads were washed 3 times with a wash buffer. After the third wash, a final
1118 centrifugation during 30 s at 2000 g was performed and the supernatant was discarded. Finally,
1119 immunoprecipitated proteins were eluted by incubating the beads with 50 uL of Laemmli buffer
1120 at 70 C for 20 min followed by 2 min centrifugation at 2500 g and recovery of the supernatant.
1121 Input and immunoprecipitated samples were analyzed by western blot.

1122 - Lipid inhibitor treatments

1123 PAO treatment was used to inhibit PI4kinases (Simon et al., 2016b). 25-30 minutes of 60µM PAO
1124 was used to 5 days old *p35S::DRONPA-s* in WT and *mctp4/3* mutants background then imaged.
1125 Wortmanin was used to inhibit PI3 kinase (Gomez et al., 2022) at a concentration of 10µM for 40
1126 minutes and YM 201653 was used to inhibit PI3,5kinase at a concentration of 2µM and treated for
1127 1 hour.

1128 - Environmental and hormonal triggers with brasinosteroids and NaCL

1129 For Brasinolide (BL) and Brassinazole (BRZ) treatment 4 days old roots of *p35S::DRONPA-s* in
1130 WT and mctp4/3 background were transferred in ½ MS plate containing 200nM BL or 1µM BRZ
1131 and grown for 24h before imaging. DMSO was used as a mock solution/ Salt treatment was
1132 performed by growing the same lines for 5 days and 20mM NaCl was applied 15 minutes before
1133 imaging. Water was used as a control solution.

1134 - Callose immunostaining

1135 Arabidopsis seedlings were vertically cultivated on ½MS agar plates for a duration of 4 days.
1136 Subsequently, they were transferred to fresh media and subjected to various treatments for an
1137 additional 24 hours. The treatments included 200 nM BR, 1 µM BRZ, DMSO mock, and a 15-
1138 minute exposure to 20mM NaCl.

1139 The immunolocalization procedure was performed following a previously published protocol
1140 (Pendle and Benitez-Alfonso, 2015). All solutions were prepared in microtubule stabilization
1141 buffer (MTSB), comprising 50 mM PIPES, 5 mM EGTA, 5 mM MgSO4, and adjusted to pH 7
1142 with KOH. Seedlings were fixed in 4% (v/v) paraformaldehyde for 1h followed by 4 washes with
1143 MTSB. Root tips were then excised and mounted on microscopy slides coated with poly-lysine.

1144 Immunolabelling was performed using the Immunorobot InSituPro VSI from Protigene. Briefly,
1145 the procedure includes cell-wall permeabilization with driselase 2% during 15 min and plasma
1146 membrane permeabilization by 10 % DMSO and 3 % Igepal during 1 h. To prevent nonspecific
1147 binding, the samples were subjected to a blocking step using 5% neutral donkey serum before
1148 incubation with the primary antibody. The callose antibody (obtained from Australia Biosupplies)
1149 was appropriately diluted to 1/500 in MTSB supplemented with 5% (v/v) neutral donkey serum
1150 and incubated with the samples at room temperature for 4 hours.

1151 For the subsequent step, the secondary anti-mouse antibody, coupled to atto550 (Merk) or alexa
1152 fluor 594, was diluted to 1/1000 in MTSB buffer containing 5% (v/v) neutral donkey serum. This
1153 antibody solution was then applied to the samples and allowed to incubate for 1 hour.

1154 - Root phenotyping

1155 *Phenotyping of the root growth rate* (Schindelin et al., 2012; Slovak et al., 2014; Platre et al., 2023)**.**
1156 Wild-type, single (*mctp3-2, mctp3-1, mctp4-1, mctp4-2, mctp6-1*), double (*mctp3-2/mctp4-1,*
1157 *mctp3-1/mctp4-1, mctp3-2/mctp6-1*) and triple (*mctp3-1/mctp4-1/mctp6-1*) mutant seeds were
1158 sowed in 12-cm x 12-cm square plates filled with 1/2 MS medium containing 0.8% of agar and
1159 0.5% of sucrose and were stratified for 2-3 days at 4°C before being transfer to a growth chamber.
1160 Six days after planting, about 20 seedlings were transferred using forceps to an imaging chamber
1161 (Lab-Tek, Chambers #1.0 Borosilicate Coverglass System, catalog number: 155361) filled with
1162 the identical medium described above. Note that the transfer took about 45-60 seconds. Images
1163 were acquired every minute for 6 hours, in brightfield conditions using a Keyence® microscope
1164 model BZ-X810 with a BZ NIKON Objective Lens 2X CFI Plan-Apo Lambda (Platre et al., 2021).
1165 The same plants were then transferred to 12-cm x 12-cm square plates filled with 1/2 MS medium
1166 containing 0.8% of agar and 0.5% of sucrose and grown to three more days and scanned to
1167 calculate the root growth rate per day.

1168 *Quantification of the root growth rate***.** For time lapse analysis of the root growth rate the script
1169 was used " SCRIPT_MCTP" and is available on https://github.com/mplatre/SCRIPT_MCTP.git.
1170 To calculate the root growth rate per day the plates were scanned using BRAT software (Slovak
1171 et al., 2014). We then calculated the root length for three days and divided by three to evaluate the
1172 root growth rate per day using Fiji (Schindelin et al., 2012).

1173 *Root hair characterization and complementation analysis.* For quantitative root hair analysis,
1174 seedling were grown in vitro, in a RH-media (2.15 g/L of MS (Duchefa, "0.5 MS"), 20 g/L of

1175 sucrose, 100 mg/L of myo-inositol, 0.5 mg/L of nicotinic acid, 0.5 mg/L of Vitamin B6, 0.1 mg/L
1176 of Vitamin B1, 2 mg/L of Glycine, 6 g/L Phytagel (Sigma-Aldrich)). Root hair length was assessed
1177 in 5-day-old seedlings, specifically focusing on homozygous T3 lines. Root hairs falling within
1178 the focal plane, spanning from 2000 µm to 4000 µm distance from the root apex, were subjected
1179 to measurement. A total of around 400 to 600 root hairs were measured for each transgenic line
1180 across two separate repetitions (approximately 200 to 300 root hairs per repetition, encompassing
1181 roughly 10 roots per repetition).

1182 - Liposome binding assays

1183 Experiment was performed as in Pérez-Sancho et al. (Pérez-sancho et al., 2016), with small
1184 modifications:

1185 *Protein production and purification*: The C2B domain of MCTP4 was expressed as His-tagged
1186 protein using the expression vector pET28 and transformed in E. Coli BL21 (DE3). A 5 mL culture
1187 of transformed bacteria in LB medium with 50 µg/mL of Kanamycin (Kan) was grown overnight
1188 at 37 °C with continuous rotation at 200 rpm. 50 mL LB medium + Kan was inoculated with 2 mL
1189 of the overnight grown culture and incubated at 37 °C for 2-3 h, until the OD600 was between 0.6
1190 and 0.8. Then, the expression of MCTP4-C2B was induced by adding 100µM IPTG to the culture
1191 and incubating overnight at 18 °C. A sample of the culture before and after protein induction was
1192 collected to assay protein production by SDS-PAGE. Cell culture was centrifuged at 1600 g during
1193 15 min and the pellet (1 g) was resuspended in 3 mL of buffer A (HEPES NaOH 50 mM pH 7.6,
1194 NaCl 150 mM, Glycerol 10%, DTT 1 mM). Cells were disrupted by sonication (three cycles of 2
1195 min, with 20 s on and 40 s off and 60 % amplitude, keeping the tube on ice) and the suspension
1196 was centrifuged at 100 000 g and 4 °C for 30 min. The supernatant was collected, mixed with 600
1197 µL of Ni-NTA beads slurry (300 µL beads) and 125 µL of Benzoase (250 U/ µL), and incubated
1198 for 1 h at 4°C wit rotation to allow proteins to bind to the beads. The mixture was centrifuged at
1199 5000 g and 4 °C for 5 min and the pelleted beads were washed 5 times with 1.5 mL of buffer A.
1200 Finally, proteins were eluted with buffer A containing 500 mM imidazole and their concentration
1201 was determined by Nanodrop (Mw 21278 and ξ 32430).

1202 *Liposome preparation:* Liposomes of different composition were prepared by mixing the
1203 corresponding lipids stocks in chloroform. Lipid stocks were: PC at 10 mg/mL, PS at 10 mg/mL,
1204 PI(4)P at 5 mg/mL, PA at 10 mg/mL, PI(4,5)P2 at 5 mg/mL, and DOPE-Rho (1,2-dioleoyl-sn-
1205 glycero-3-phosphoethanolamine conjugated to rhodamine) at 1 mg/mL (used to visualize the lipid
1206 fraction during the preparation); and were mixed as indicated in the table below:

1207

	PC (µL)	PS (µL)	PI(4)P (µL)	PA (µL)	PI(4,5)P2 (µL)	DOPE-Rho (µL)
PC	78	0	0	0	0	13
PC:PS	62	20	0	0	0	13
PC:PS:PI(4)P	42	20	40	0	0	13

PC:PS:PA	50	20	0	7	0	13
PC:PS:PI(4,5)P2	42	20	0	0	44	13

Lipid mixtures were dried as a thin layer using a nitrogen stream and the lipid layers were resuspended in 1 mL of buffer A by vortexing at room temperature during 20 min. Then, they were subjected to 5 cycles of freezing in liquid nitrogen and thawing in a water bath at 37 °C and extruded 10 times through an 800 nm pore size polycarbonate membrane.

Liposome binding and sedimentation: 10 µg of purified MCTP4-C2B and 40 µL of liposomes were mixed in buffer A containing 10 mM CaCl2 (1 mix for each different liposome composition) until a final volume of 200 µL and incubated at room temperature for 15 min without agitation. Large multilamellar vesicles (and the proteins bound to them) were collected by centrifugation at 300 000 g and 4°C for 45 min. 195 µL of supernatants were recovered and the pellets were resuspended in 195 µL of buffer A. Supernatant and resuspended-pellet fractions were mix with Coomassie blue buffer and run into SDS-PAGE for protein separation and quantification. Only one band corresponding to the C2B domain of MCTP4 was observed for each of the samples and each of the repetitions of the experiment. Gels were imaged using a Bio-rad's stain-free imager on TGX-Stain-Free acrylamide gels and proteins quantified using Fiji.

- Plasmodesmata purification and lipid analysis via liquid chromatography-tandem mass spectrometry (LC-MS/MS)

The cell wall fractions were prepared from 6-day-old Arabidopsis suspension cultured cells, following the methodology outlined by Bayer et al. (Bayer et al., 2004). However, in this study, the cell disruption process was repeated five consecutive times using the N2 cell disruption vessel, in contrast to the standard three repetitions. To obtain the plasmodesmata-enriched membrane fraction, purified wall fragments were utilized, employing the method described by (Fouillen et al., 2022). Briefly, purified cell walls were subjected to digestion with 0.7% (w/v) cellulase R10 (Karlan) in a digestion buffer comprising 10 mM MES (pH 5.5) and 4.4% mannitol, supplemented with 1 µM phenylmethylsulfonyl fluoride and a complete protease inhibitor cocktail (Roche Diagnostic). The digestion process was carried out at 37°C for 1.5 hours with continuous shaking at 50 to 100 rpm. Following the digestion step, centrifugation was performed at 5850g for 5 minutes at 4°C to separate the supernatant and pellet fractions. The pellet underwent additional washing in an excess volume of digestion buffer before undergoing a second centrifugation step. The two supernatants were combined and subjected to further centrifugation at 110,000g for 40 minutes at 4°C. The resulting pellet, which contained plasmodesmata-derived membranes, was washed with an excess volume of cold Tris-buffered saline (TBS; 20 mM Tris-HCl, 0.14 M NaCl, and 2.5 mM KCl, pH 7.4). Finally, the pellet was resuspended in cold 1× TBS containing protease inhibitors (Roche Diagnostic). It is noteworthy that approximately 600 mL of cultured cells was employed to yield 100 µg of plasmodesmata-enriched membrane fraction. The protein amount in

1245 the samples was determined using a bicinchoninic acid protein assay with BSA as the standard.
1246 For the purification of plasmodesmata-enriched membrane fractions from cells subjected to sterol
1247 inhibitor treatment, fen was added to 5-day-old liquid cultured Arabidopsis cells at a final
1248 concentration of 250 µg/mL (stock solution 500 µg/µL in DMSO) and incubated as previously
1249 described for 48 hours before the purification process.

1250 For anionic lipid analysis we followed the protocol described in (Genva et al., 2023). In brief,
1251 plasmodesmata fraction was incubated with 725 µL of a MeOH/$CHCl_3$/1M HCl (2/1/0.1 v/v/v)
1252 solution and 150 µL water in presence of 10 ng of 17:0-20:4 PI(4)P standard (Avanti). 750 µl of
1253 chloroform and 170 µl HCl 2M were then added. The samples were vigorously shaken and
1254 centrifuged. The lower phase was washed with 700 µl of the upper phase of a mix of
1255 methanol:chloroform:HCl 0.01M 1:2:0.75, vortexed and centrifuged. Then, samples were kept
1256 overnight at -20 °C.

1257 The organic phase was transferred to a new Eppendorf and the methylation reaction was carried
1258 out. For this purpose, 50 µL of TMS-diazomethane (2M in hexane) were added to each sample.
1259 After 10 min, the reaction was stopped by adding 6 µL of glacial acetic acid. 700 µL of the upper
1260 phase of a mix of MeOH/$CHCl_3$/H_2O (1/2/0.75 v/v/v) was added to each sample which was then
1261 vortexed and centrifuged (1500 x *g*, 3 min). The upper phase was removed and the washing step
1262 was repeated once. Finally, the lower organic phases were transferred to a new Eppendorf.
1263 Following the addition of 100 µL MeOH/H2O (9:1 v/v), the samples were concentrated under a
1264 gentle flow of air until only a drop remained. 80 µL of methanol were added to the samples, which
1265 were submitted to ultrasounds for 1 minute, before adding 20 µL water, and were submitted to 1
1266 more-minute ultrasound. The samples were finally transferred to HPLC vials for analysis.

1267 Analysis of methylated anionic phospholipids (Genva et al., 2023) were performed using a liquid
1268 chromatography system (1290 Infinity II, Agilent) coupled to a QTRAP 6500 mass spectrometer
1269 (ABSciex). The chromatographic separation of anionic phospholipid species was performed on a
1270 reverse phase C18 column (SUPELCOSIL ABZ PLUS; 10 cm x 2.1 mm, 3µm, Merck) using
1271 methanol/water (3/2) as solvent A and isopropanol/methanol (4/1) as solvent B at a flow rate of
1272 0.2 mL/min. All solvents are supplemented with 0.1% HCCOOH and 10 mM ammonium formate.
1273 10 µL of samples were injected and the percentage of solvent B during the gradient elution was
1274 the following: 0–20 min, 45%; 40 min, 60%; 50 min, 80%. The column temperature was kept at
1275 40 °C. Mass spectrometry analysis was performed in the positive ionization mode. Mass
1276 spectrometry data were treated using the MultiQuant software (ABSciex). Nitrogen was used for
1277 the curtain gas (set to 35), gas 1 (set to 40), and gas 2 (set to 40). Needle voltage was at +5500 V
1278 with needle heating at 350 °C; the declustering potential was +10 V. The collision gas was also
1279 nitrogen; it was set between 26 to 45 eV according to the lipid classes.

1280 - Identification of peptides by mass spectrometry.

1281 Each sample was deposited on a 10% acrylamide SDS-PAGE. After a short migration, gels were
1282 stained with colloidal blue overnight. The bands of interest from the SDS-PAGE gel were cut and
1283 destained. Reduction of disulfide bonds and alkylation of cysteine were performed, and proteins
1284 were finally digested overnight with trypsin. Resulting peptides were extracted from the gel,
1285 acidified and were injected on a Ultimate 3000 nanoLC system (Dionex, Amsterdam, The
1286 Netherlands) coupled to a Electrospray Orbitrap Fusion™ Lumos™ Tribrid™ Mass Spectrometer
1287 (Thermo Fisher Scientific, San Jose, CA). The spectra obtained were analyzed by Proteome
1288 Discoverer 3.1 with Sequest HT as the search algorithm, using an *Arabidopsis thaliana* protein
1289 database (Araport_20220103; 40,668 entries), including 2 missed cleavage sites by trypsin,
1290 carbamidomethylation of cysteine (+57 Da) as static modification) and oxidation of methionine
1291 (+16 Da), acetylation of protein N-term (+42 Da), Methionine loss (-131 Da) methionine
1292 loss/acetylation (+89 Da) as dynamic modification. Peptide validation was performed using
1293 Percolator algorithm and only "high confidence" peptides were retained corresponding to a 1%
1294 False Positive Rate at peptide level. Peaks were detected and integrated using the Minora algorithm
1295 embedded in Proteome Discoverer.

1296 Protein abundances ware calculated as the sum of the abundance of corresponding unique peptides.
1297 Normalization was performed based on total *Arabidopsis thaliana* protein amount. Protein ratios
1298 were calculated as the median of all possible pairwise peptide ratios. A t-test was calculated based
1299 on background population of peptides or proteins. Quantitative data were considered for proteins
1300 quantified by a minimum of two peptides and a statistical p-value lower than 0.05.

1301 - Molecular dynamics

1302 *Membrane Creation:* We used the Insane program (Jumper et al., 2021) to generate three
1303 membranes with a composition representative of the plasma membrane: (70%,68%,64%)
1304 phosphatidylcholine (PC), 20% Sitosterol, 10% phosphatidylserine (PS), (0%, 2%, 6%) PI(4)P.
1305 Two lipids present in our modeled membrane were not present in the Martini 3 topology library:
1306 PS of plants that have a longer tail (18:2 24:1) and sitosterol. The topology for PS (18:2 24:1) was
1307 created by analogy, using the topology files of PIPS and DNPS. The Sitosterol model was obtained
1308 from Paulo C. T. Souza and Luís Borges Araújo following the recent parameterization of
1309 cholesterol in MARTINI 3 (Borges-Araújo et al., 2023).

1310 *Protein Setup*: Three prediction tools, AlphaFold Monomer (Jumper et al., 2021), AlphaFold
1311 Multimer (Souza et al., 2021), and RosettaFold (Baek et al., 2021), were employed to determine the
1312 3D structure of MCTP4. These methods converged on a single solution for the C2 domains.

1313 All simulations were conducted using Gromacs 2021.5
1314 (https://manual.gromacs.org/2021.5/release-notes/index.html), supplemented with the Colvar
1315 plugin (Fiorin et al., 2013). The Martini 3 force field (Souza et al., 2021) was utilized. We applied
1316 a constraint network to the protein to stabilize the 3D structure of the cytoplasmic domain. The
1317 protein's center of mass was positioned 10 nm from the membrane. We replicated each condition

five times. Each system underwent minimization and equilibration at 300K. The protocol included an initial phase of energy minimization, followed by multi-stage equilibration, and concluded with a production simulation. Energy minimization was performed in two iterations of 5,000 steps each, using the steepest descent method. The simulations were then equilibrated in five stages, using time steps of 2, 5, 10, 15, and 20 fs. A target temperature of 300 K was maintained using the v-rescale thermostat, with a coupling constant of 1 ps. A semi-isotropic pressure of 1 bar was maintained using the Parrinello-Rahman barostat, with a compressibility of 4.5 × 10^-5 bar^-1 and a relaxation time constant of 12 ps. Long-range interactions were handled with a cutoff radius of 1.1 nm for both van der Waals and Coulombic interactions, implementing a switching function from 1.0 nm for van der Waals. The production simulations were executed in an NPT ensemble with a time step of 20 fs for a total simulation time of 3 microseconds.

Simulation Condition

- Colvars

Two collective variables (colvars) were used to maintain a realistic orientation of the protein relative to the membrane. The colvar tilt was chosen to control the protein's tilt angle, and the colvar distanceZ was implemented to prevent the protein from passing through the periodic box.

- Protein Variants

Specific mutations were introduced to study their impact on the functionality and interaction of proteins with membranes. These mutations were identified by analyzing contacts in our simulations with PI4P and using a prediction tool for membrane-interacting residues, hydrophobic protrusions (https://reuter-group.github.io/peprmint/pepr2vis).
The following mutations were explored:
Five residues on the C2C domain (D217N, K218Q, R220Q, K318Q, K322Q).
To observe the effect of the presence or absence of PI4P on the interaction of the protein with the membrane we performed simulations with various PI4P concentrations (without PI4P or with a 2% concentration of PI4P). Then to assess the impact of these modifications on the domain of the protein, we perform simulations C2C variant. In each case, all three domains of the protein were retained in the mutants to ensure a comprehensive analysis.

- Calculation of Minimum Distances

To evaluate interactions between mutated proteins and PI4P molecules, the minimum distance between the mutated regions of the proteins and PI4P was calculated using the gmx mindist tool from GROMACS. In the condition without PI4P we compute the distance with the membrane.

1356 - Distance Analysis
1357
1358 The minimum distances obtained were used to generate a histogram representing the distribution
1359 of observed distances. The distance histogram was divided into several bins (distance intervals).
1360 The first bin, representing the shortest distances (>0.5nm), was specifically analyzed to identify
1361 the closest contacts between proteins and PI4P. The contact distances calculated with gmx for each
1362 domain (C2B, C2C, and C2D) were obtained as previously described in the minimum distance
1363 section. We performed an ANOVA test to statistically evaluate these contacts, ensuring all
1364 conditions such as homogeneity of variances and normality were met.
1365

1366 - Quantification and Statistical Analysis

1367 Statistical analyses were performed in GraphPad Prism (GraphPad Software). All experiments
1368 were independently repeated a minimum of 2–3 times (indicated in figure legends). Data are
1369 expressed as median unless specified in the figure legends.

1370 **References**

1371 **Abou-Saleh RH, Hernandez-Gomez MC, Amsbury S, Paniagua C, Bourdon M, Miyashima S,**
1372 **Helariutta Y, Fuller M, Budtova T, Connell SD, et al** (2018) Interactions between callose and
1373 cellulose revealed through the analysis of biopolymer mixtures. Nat Commun **9**: 4538

1374 **Amari K, Boutant E, Hofmann C, Schmitt-Keichinger C, Fernandez-Calvino L, Didier P, Lerich A,**
1375 **Mutterer J, Thomas CL, Heinlein M, et al** (2010) A family of plasmodesmal proteins with
1376 receptor-like properties for plant viral movement proteins. PLoS Pathog **6**: 1–10

1377 **Amsbury S, Kirk P, Benitez-Alfonso Y** (2017) Emerging models on the regulation of intercellular
1378 transport by plasmodesmata-associated callose. J Exp Bot **69**: 105–115

1379 **Baek M, DiMaio F, Anishchenko I, Dauparas J, Ovchinnikov S, Lee GR, Wang J, Cong Q, Kinch**
1380 **LN, Dustin Schaeffer R, et al** (2021) Accurate prediction of protein structures and interactions
1381 using a three-track neural network. Science (80-) **373**: 871–876

1382 **Balla T** (2018) Ca2+ and lipid signals hold hands at endoplasmic reticulum–plasma membrane contact
1383 sites. J Physiol **596**: 2709–2716

1384 **Bayer E, Thomas CLL, Maule AJJ** (2004) Plasmodesmata in Arabidopsis thaliana suspension cells.
1385 Protoplasma **223**: 93–102

1386 **Benavente JL, Siliqi D, Infantes L, Lagartera L, Mills A, Gago F, Ruiz-López N, Botella MA,**
1387 **Sánchez-Barrena MJ, Albert A** (2021) The structure and flexibility analysis of the Arabidopsis
1388 synaptotagmin 1 reveal the basis of its regulation at membrane contact sites. Life Sci Alliance. doi:
1389 10.26508/LSA.202101152

1390 **Benitez-Alfonso Y, Faulkner C, Pendle A, Miyashima S, Helariutta Y, Maule A** (2013) Symplastic
1391 intercellular connectivity regulates Llteral root patterning. Dev Cell **26**: 136–147

1392 **Bharathan NK, Giang W, Hoffman CL, Aaron JS, Khuon S, Chew TL, Preibisch S, Trautman ET,**
1393 **Heinrich L, Bogovic J, et al** (2023) Architecture and dynamics of a desmosome–endoplasmic
1394 reticulum complex. Nat Cell Biol **25**: 823–835

1395 **Bian X, Saheki Y, De Camilli P** (2018) Ca 2+ releases E-Syt1 autoinhibition to couple ER -plasma
1396 membrane tethering with lipid transport . EMBO J **37**: 219–234

1397 **Borges-Araújo L, Borges-Araújo AC, Ozturk TN, Ramirez-Echemendia DP, Fábián B, Carpenter**
1398 **TS, Thallmair S, Barnoud J, Ingólfsson HI, Hummer G, et al** (2023) Martini 3 Coarse-Grained
1399 Force Field for Cholesterol. J Chem Theory Comput. doi: 10.1021/acs.jctc.3c00547

1400 **Brault ML, Petit JD, Immel F, Nicolas WJ, Glavier M, Brocard L, Gaston A, Fouché M, Hawkins**
1401 **TJ, Crowet J-M, et al** (2019) Multiple C2 domains and transmembrane region proteins (MCTPs)
1402 tether membranes at plasmodesmata. EMBO Rep e47182

1403 **Cheval C, Faulkner C** (2018) Plasmodesmal regulation during plant–pathogen interactions. New Phytol
1404 **217**: 62–67

1405 **Chung J yun, Torta F, Masai K, Lucast L, Czapla H, Tanner LB, Narayanaswamy P, Wenk MR,**
1406 **Nakatsu F, De Camilli P, et al** (2015) PI4P/phosphatidylserine countertransport at ORP5- and
1407 ORP8-mediated ER – plasma membrane contacts. Science (80-) **349**: 428–432

1408 **Clough SJ, Bent AF** (1998) Floral dip : a simplified method for Agrobacterium-mediated transformation
1409 of Arabidopsis thaliana. Plant J **16**: 735–743

1410 **Collado J, Kalemanov M, Martinez-Sanchez A, Campelo F, Baumeister W, Stefan CJ, Fernandez-**
1411 **Busnadiego R** (2019) Tricalbin-Mediated Contact Sites Control ER Curvature to Maintain Plasma
1412 Membrane Integrity. SSRN Electron J 1–61

1413 **Crawford KM, Zambryski PC** (2001) Non-targeted and targeted protein movement through
1414 plasmodesmata in leaves in different developmental and physiological states. Plant Physiol **125**:
1415 1802–1812

1416 **Cui W, Lee J-YY** (2016) Arabidopsis callose synthases CalS1/8 regulate plasmodesmal permeability
1417 during stress. Nat Plants **2**: 16034

1418 **Daum G, Medzihradszky A, Suzaki T, Lohmann JU** (2014) A mechanistic framework for non-cell
1419 autonomous stem cell induction in Arabidopsis. Proc Natl Acad Sci U S A **111**: 14619–24

1420 **Deinum EE, Mulder BM, Benitez-Alfonso Y** (2019) From plasmodesma geometry to effective
1421 symplasmic permeability through biophysical modelling. Elife **8**: 1–40

1422 **Ding B, Turgeon R, Parthasarathy M V.** (1992) Substructure of freeze-substituted plasmodesmata.
1423 Protoplasma **169**: 28–41

1424 **Dong R, Saheki Y, Swarup S, Lucast L, Harper JW, De Camilli P** (2016) Endosome-ER contacts
1425 control actin nucleation and retromer function through VAP-dependent regulation of PI4P. Cell **166**:
1426 408–423

1427 **Dubois GA, Jaillais Y** (2021) Anionic phospholipid gradients: An uncharacterized frontier of the plant
1428 endomembrane network. Plant Physiol **185**: 577–592

1429 **Eden ER, Sanchez-Heras E, Tsapara A, Sobota A, Levine TP, Futter CE** (2016) Annexin A1 tethers
1430 membrane contact sites that mediate ER to endosome cholesterol transport. Dev Cell **37**: 473–483

1431 **Eden ER, White IJ, Tsapara A, Futter CE** (2010) Membrane contacts between endosomes and ER
1432 provide sites for PTP1B-epidermal growth factor receptor interaction. Nat Cell Biol **12**: 267–72

1433 **Faulkner C, Petutschnig E, Benitez-Alfonso Y, Beck M, Robatzek S, Lipka V, Maule AJ** (2013)
1434 LYM2-dependent chitin perception limits molecular flux via plasmodesmata. Proc Natl Acad Sci U
1435 S A **110**: 9166–70

1436 **Fernandez-Calvino L, Faulkner C, Walshaw J, Saalbach G, Bayer E, Benitez-Alfonso Y, Maule A**
1437 (2011) Arabidopsis plasmodesmal proteome. PLoS One **6**: e18880

1438 **von Filseck JM, Vanni S, Mesmin B, Antonny B, Drin G** (2015) A phosphatidylinositol-4-phosphate
1439 powered exchange mechanism to create a lipid gradient between membranes. Nat Commun **6**: 1–12

1440 **Fiorin G, Klein ML, Hénin J** (2013) Using collective variables to drive molecular dynamics
1441 simulations. Mol Phys **111**: 3345–3362

1442 **Fouillen L, Claverol S, Bayer E, Grison SM** (2022) Isolation of plasmodesmata membranes for
1443 lipidomic and proteomic analysis. Method Mol Biol **2457**: 189–207

1444 **Friedman JR, Lackner LL, West M, DiBenedetto JR, Nunnari J, Voeltz GK** (2011) ER tubules mark
1445 sites of mitochondrial division. Science (80-) **334**: 358–362

1446 **Gao C, Liu X, Storme N De, Martens HJ, Schulz A, Liesche J, Gao C, Liu X, Storme N De, Jensen**
1447 **KH, et al** (2020) Directionality of Plasmodesmata-Mediated Transport in Arabidopsis Leaves
1448 Supports Auxin Report Directionality of Plasmodesmata-Mediated Transport in Arabidopsis Leaves
1449 Supports Auxin Channeling. Curr Biol **30**: 1970-1977.e4

1450 **Gaudioso-Pedraza R, Beck M, Frances L, Kirk P, Ripodas C, Niebel A, Oldroyd GEDD, Benitez-**
1451 **alfonso Y, de Carvalho-Niebel F, Carvalho-niebel F De, et al** (2018) Callose-regulated
1452 symplastic communication coordinates symbiotic root nodule development. Curr Biol **28**: 3562-
1453 3577.e6

1454 **Genva M, Fougère L, Bahammou D, Mongrand S, Boutté Y, Fouillen L** (2023) A global LC–MS2-
1455 based methodology to identify and quantify anionic phospholipids in plant samples. Plant J. doi:
1456 10.1111/tpj.16525

1457 **Gerlitz N, Gerum R, Sauer N, Stadler R** (2018) Photoinducible DRONPA-s : a new tool for
1458 investigating cell – cell connectivity. Plant Physiol **94**: 751–766

1459 **Giordano F, Saheki Y, Idevall-Hagren O, Colombo SF, Pirruccello M, Milosevic I, Gracheva EO,**
1460 **Bagriantsev SN, Borgese N, De Camilli P** (2013) PI(4,5)P2-dependent and Ca2+-regulated ER-
1461 PM interactions mediated by the extended synaptotagmins. Cell **153**: 1494

1462 **Gisel A, Barella S, Hempel FD, Zambryski PC** (1999) Temporal and spatial regulation of symplastic
1463 trafficking during development in Arabidopsis thaliana apices. Development **126**: 1879–1889

1464 **Gombos S, Miras M, Howe V, Xi L, Pottier M, Kazemein Jasemi NS, Schladt M, Ejike JO,**
1465 **Neumann U, Hänsch S, et al** (2023) A high-confidence Physcomitrium patens plasmodesmata
1466 proteome by iterative scoring and validation reveals diversification of cell wall proteins during
1467 evolution. New Phytol **238**: 637–653

1468 **Grison MS, Kirk P, Brault ML, Wu XN, Schulze WX, Benitez-Alfonso Y, Immel F, Bayer EM**
1469 (2019) Plasma membrane-associated receptor-like kinases relocalize to plasmodesmata in response
1470 to osmotic stress. Plant Physiol. doi: 10.1104/pp.19.00473

1471 **Guenoune-Gelbart D, Elbaum M, Sagi G, Levy A, Epel BL** (2008) Tobacco mosaic virus (TMV)
1472 replicase and movement protein function synergistically in facilitating TMV spread by lateral
1473 diffusion in the plasmodesmal desmotubule of Nicotiana benthamiana. Mol Plant Microbe Interact
1474 **21**: 335–345

1475 **Guillén-Samander A, De Camilli P** (2023) Endoplasmic reticulum membrane contact sites, lipid
1476 transport, and neurodegeneration. Cold Spring Harb Perspect Biol. doi:

1477 10.1101/cshperspect.a041257

1478 **Guseman JM, Lee JS, Bogenschutz NL, Peterson KM, Virata RE, Xie B, Kanaoka MM, Hong Z,**
1479 **Torii KU** (2010) Dysregulation of cell-to-cell connectivity and stomatal patterning by loss-of-
1480 function mutation in Arabidopsis CHORUS (GLUCAN SYNTHASE-LIKE 8). Development **137**:
1481 1731–1741

1482 **Hamasaki M, Furuta N, Matsuda A, Nezu A, Yamamoto A, Fujita N, Oomori H, Noda T,**
1483 **Haraguchi T, Hiraoka Y, et al** (2013) Autophagosomes form at ER-mitochondria contact sites.
1484 Nature **495**: 389–393

1485 **Han X, Hyun T, Zhang M, Kumar R, Koh EJ, Kang BH, Lucas W, Kim JY** (2014) Auxin-callose-
1486 mediated plasmodesmal gating is essential for tropic auxin gradient formation and signaling. Dev
1487 Cell **28**: 132–146

1488 **Hernández-Alvarez MI, Sebastián D, Vives S, Ivanova S, Bartoccioni P, Kakimoto P, Plana N,**
1489 **Veiga SR, Hernández V, Vasconcelos N, et al** (2019) Deficient endoplasmic reticulum-
1490 mitochondrial phosphatidylserine transfer causes liver disease. Cell **177**: 881-895.e17

1491 **Hirabayashi Y, Kwon SK, Paek H, Pernice WM, Paul MA, Lee J, Erfani P, Raczkowski A, Petrey**
1492 **DS, Pon LA, et al** (2017) ER-mitochondria tethering by PDZD8 regulates Ca2+ dynamics in
1493 mammalian neurons. Science (80-) **358**: 623–630

1494 **Hoffmann PC, Bharat TAM, Wozny MR, Boulanger J, Miller EA, Kukulski W** (2019) Tricalbins
1495 Contribute to Cellular Lipid Flux and Form Curved ER-PM Contacts that Are Bridged by Rod-
1496 Shaped Structures. Dev Cell **51**: 488-502.e8

1497 **Hunter K, Kimura S, Rokka A, Tran HC, Toyota M, Kukkonen JP, Wrzaczek M** (2019) CRK2
1498 enhances salt tolerance by regulating callose deposition in connection with PLDα1. Plant Physiol.
1499 doi: 10.1104/pp.19.00560

1500 **Jaillais Y, Belkhadir Y, Balsemão-Pires E, Dangl JL, Chory J** (2011) Extracellular leucine-rich
1501 repeats as a platform for receptor/coreceptor complex formation. Proc Natl Acad Sci U S A **1**: 1–5

1502 **Johnson B, Iuliano M, Lam T, Biederer T, De Camilli P** (2023) A complex of the lipid transport ER
1503 proteins TMEM24 and C2CD2 with band 4.1 at cell-cell contacts. An ER-plasma membrane
1504 complex at cell contacts. bioRxiv. doi: 10.1101/2023.12.06.570396

1505 **Johnston MG, Breakspear A, Samwald S, Zhang D, Papp D, Faulkner C, De Keijzer J** (2023)
1506 Comparative phyloproteomics identifies conserved plasmodesmal proteins. J Exp Bot **74**: 1821–
1507 1835

1508 **Jumper J, Evans R, Pritzel A, Green T, Figurnov M, Ronneberger O, Tunyasuvunakool K, Bates**
1509 **R, Žídek A, Potapenko A, et al** (2021) Highly accurate protein structure prediction with
1510 AlphaFold. Nature **596**: 583

1511 **Kalmbach, L., Bourdon, M., Belevich, I., Safran, J., Lemaire, A., Heo, J.-o., Otero, S., Blob, B.,**
1512 **Pelloux, J., Jokitalo, E., and Helariutta, Y. (2023)**. Putative pectate lyase PLL12 and callose
1513 deposition through polar CALS7 are necessary for long-distance phloem transport in Arabidopsis.

1514 Current Biology 33, 926-939.e929.

1515 **Karimi, M., Bleys, A., Vanderhaeghen, R., and Hilson, P.** (2007). Building blocks for plant gene
1516 assembly. Plant Physiol 145, 1183-1191. 10.1104/pp.107.110411.

1517 **Kirk P, Amsbury S, German L, Gaudioso-Pedraza R, Benitez-Alfonso Y** (2022) A comparative meta-
1518 proteomic pipeline for the identification of plasmodesmata proteins and regulatory conditions in
1519 diverse plant species. BMC Biol **20**: 1–21

1520 **Kitagawa M, Wu P, Balkunde R, Cunniff P, Jackson D** (2022) An RNA exosome subunit mediates
1521 cell-to-cell trafficking of a homeobox mRNA via plasmodesmata. Science (80-) **375**: 177–182

1522 **Koulouras G, Panagopoulos A, Rapsomaniki MA, Giakoumakis NN, Taraviras S, Lygerou Z** (2018)
1523 EasyFRAP-web: A web-based tool for the analysis of fluorescence recovery after photobleaching
1524 data. Nucleic Acids Res **46**: W467–W472

1525 **Kraner ME, Müller C, Sonnewald U** (2017) Comparative proteomic profiling of the choline
1526 transporter-like1 (CHER1) mutant provides insights into plasmodesmata composition of fully
1527 developed Arabidopsis thaliana leaves. Plant J **92**: 696–709

1528 **Kumagai K, Hanada K** (2019) Structure, functions and regulation of CERT, a lipid-transfer protein for
1529 the delivery of ceramide at the ER–Golgi membrane contact sites. FEBS Lett **593**: 2366–2377

1530 **Lebecq A, Doumane M, Fangain A, Bayle V, Leong JX, Rozier F, Del Marques-Bueno M,**
1531 **Armengot L, Boisseau R, Simon ML, et al** (2022) The Arabidopsis SAC9 enzyme is enriched in a
1532 cortical population of early endosomes and restricts PI(4,5)P2 at the plasma membrane. Elife. doi:
1533 10.7554/eLife.73837

1534 **Lee E, Vanneste S, Pérez-Sancho J, Benitez-Fuente F, Strelau M, Macho AP, Botella MA, Friml J,**
1535 **Rosado A** (2019a) Ionic stress enhances ER–PM connectivity via phosphoinositide-associated
1536 SYT1 contact site expansion in Arabidopsis. Proc Natl Acad Sci U S A **116**: 1420–1429

1537 **Lee E, Vanneste S, Pérez-Sancho J, Benitez-Fuente F, Strelau M, Macho AP, Botella MA, Friml J,**
1538 **Rosado A** (2019b) Ionic stress enhances ER–PM connectivity via phosphoinositide-associated
1539 SYT1 contact site expansion in Arabidopsis. Proc Natl Acad Sci U S A **116**: 1420–1429

1540 **Lee EK, Santana BVN, Samuels E, Benitez-Fuente F, Corsi E, Botella MA, Perez-Sancho J,**
1541 **Vanneste S, Friml J, Macho A, et al** (2020) Rare earth elements induce cytoskeleton-dependent
1542 and PI4P-associated rearrangement of SYT1/SYT5 endoplasmic reticulum-plasma membrane
1543 contact site complexes in Arabidopsis. J Exp Bot **71**: 3986–3998

1544 **Lees JA, Messa M, Sun EW, Wheeler H, Torta F, Wenk MR, De Camilli P, Reinisch KM** (2017)
1545 Lipid transport by TMEM24 at ER-plasma membrane contacts regulates pulsatile insulin secretion.
1546 Science (80-). doi: 10.1126/science.aah6171

1547 **Lexy RO, Kasai K, Clark N, Fujiwara T, Sozzani R, Gallagher KL** (2018) Exposure to heavy metal
1548 stress triggers changes in plasmodesmatal permeability via deposition and breakdown of callose. **69**:
1549 3715–3728

1550 **Li ZP, Moreau H, Petit JD, Souza-Moraes T, Smokvarska M, Perez-Sancho J, Petrel M, Decoeur F,**
1551 **Brocard L, Chambaud C, et al** (2023) Plant plasmodesmata bridges form through ER-driven
1552 incomplete cytokinesis. bioRxiv

1553 **Li ZP, Paterlini A, Glavier M, Bayer EM** (2021) Intercellular trafficking via plasmodesmata: molecular
1554 layers of complexity. Cell Mol Life Sci **78**: 799–816

1555 **Marković V, Jaillais Y** (2022) Phosphatidylinositol 4-phosphate: a key determinant of plasma membrane
1556 identity and function in plants. New Phytol **235**: 867–874

1557 **Marquès-Bueno MM, Morao AK, Cayrel A, Platre MP, Barberon M, Caillieux E, Colot V, Jaillais**
1558 **Y, Roudier F, Vert G** (2016) A versatile Multisite Gateway-compatible promoter and transgenic
1559 line collection for cell type-specific functional genomics in Arabidopsis. Plant J **85**: 320–333

1560 **Mehra P, Pandey BK, Melebari D, Banda J, Leftley N, Couvreur V, Rowe J, Anfang M, De Gernier**
1561 **H, Morris E, et al** (2022) Hydraulic flux–responsive hormone redistribution determines root
1562 branching. Science (80-) **378**: 762–768

1563 **Mellor NL, Voß U, Janes G, Bennett MJ, Wells DM, Band LR** (2020) Auxin fluxes through
1564 plasmodesmata modify root-tip auxin distribution. Development. doi: 10.1242/dev.181669

1565 **Mesmin B, Bigay J, Von Filseck JM, Lacas-Gervais S, Drin G, Antonny B** (2013) A four-step cycle
1566 driven by PI(4)P hydrolysis directs sterol/PI(4)P exchange by the ER-Golgi Tether OSBP. Cell **155**:
1567 830–843

1568 **Mesmin B, Bigay J, Polidori J, Jamecna D, Lacas-Gervais S, Antonny B** (2017) Sterol transfer, PI4P
1569 consumption, and control of membrane lipid order by endogenous OSBP. EMBO J **36**: e201796687

1570 **Miras M, Pottier M, Schladt TM, Ejike JO, Redzich L, Frommer WB, Kim JY** (2022a)
1571 Plasmodesmata and their role in assimilate translocation. J Plant Physiol **270**: 153633

1572 **Miras M, Pottier M, Schladt TM, Ejike JO, Redzich L, Frommer WB, Kim JY** (2022b)
1573 Plasmodesmata and their role in assimilate translocation. J Plant Physiol **270**: 153633

1574 **Miyashima S, Roszak P, Sevilem I, Toyokura K, Blob B, Heo J, Mellor N, Help-rinta-rahko H,**
1575 **Otero S, Smet W, et al** (2019) Mobile PEAR transcription factors integrate positional cues to prime
1576 cambial growth. Nature **565**: 490–494

1577 **Nakajima K, Sena G, Nawy T, Benfey PN** (2001) Intercellular movement of the putative transcription
1578 factor SHR in root patterning. Nature **413**: 307–311

1579 **Naón D, Hernández-Alvarez MI, Shinjo S, Wieczor M, Ivanova S, de Brito OM, Quintana A,**
1580 **Hidalgo J, Palacín M, Aparicio P, et al** (2023) Splice variants of mitofusin 2 shape the
1581 endoplasmic reticulum and tether it to mitochondria. Science (80-). doi: 10.1126/science.adh9351

1582 **Nicolas W, Grison M, Trépout S, Gaston A, Fouché M, Cordelières F, Oparka K, Tilsner J,**
1583 **Brocard L, Bayer E** (2017a) Architecture and permeability of post-cytokinesis plasmodesmata
1584 lacking cytoplasmic sleeve. Nat Plants **3**: 17082

1585 **Nicolas W, Grison MS, Bayer EMF** (2017b) Shaping intercellular channels of plasmodesmata: the
1586 structure-to-function missing link. J Exp Bot **69**: 91–103

1587 **Noack LC, Jaillais Y** (2020) Functions of anionic lipids in plants. Annu Rev Plant Biol **71**: 71–102

1588 **Ostermeyer GP, Jensen KH, Franzen AR, Peters WS, Knoblauch M** (2022) Diversity of funnel
1589 plasmodesmata in angiosperms: the impact of geometry on plasmodesmal resistance. Plant J **110**:
1590 707–719

1591 **Otero S, Helariutta Y, Benitez-Alfonso Y** (2016) Symplastic communication in organ formation and
1592 tissue patterning. Curr Opin Plant Biol **29**: 21–28

1593 **Pain C, Kriechbaumer V, Kittelmann M, Hawes C, Fricker M** (2019) Quantitative analysis of plant
1594 ER architecture and dynamics. Nat Commun **10**: 1–15

1595 **Pérez-sancho J, Schapire AL, Botella MA, Rosado A** (2016) Analysis of protein-Lipid interactions
1596 using purified C2 domains. Methods Mol Biol **1363**: 175–187

1597 **Pérez-Sancho J, Vanneste S, Lee E, McFarlane H, Esteban del Valle A, Valpuesta V, Friml J,**
1598 **Botella MA, Rosado A** (2015a) The Arabidopsis SYT1 is enriched in ER-PM contact sites and
1599 confers cellular resistance to mechanical stresses. Plant Physiol **168**: 132–143

1600 **Pérez-Sancho J, Vanneste S, Lee E, McFarlane HE, Esteban Del Valle A, Valpuesta V, Friml J,**
1601 **Botella MA, Rosado A** (2015b) The Arabidopsis synaptotagmin1 is enriched in endoplasmic
1602 reticulum-plasma membrane contact sites and confers cellular resistance to mechanical stresses.
1603 Plant Physiol **168**: 132–43

1604 **Petit JD, Glavier M, Brocard L, Bayer EM** Plasmodesmata ultrastructure determination using electron
1605 tomography. Method Mol. Biol.

1606 **Platre MP, Mehta P, Halvorson Z, Zhang L, Brent L, Gleason F. M, Faizi K, Goulding C, Busch W**
1607 (2023) Root Walker: an automated pipeline for large scale quantification of early root growth
1608 responses at high spatial and temporal resolution. Plant J. doi: 10.1111/tpj.16493

1609 **Platre MP, Noack LC, Doumane M, Bayle V, Simon MLA, Maneta-Peyret L, Fouillen L, Stanislas**
1610 **T, Armengot L, Pejchar P, et al** (2018) A Combinatorial lipid code shapes the electrostatic
1611 landscape of plant endomembranes. Dev Cell **45**: 465-480.e11

1612 **Platre MP, Satbhai SB, Brent L, Gleason MF, Cao M, Grison M, Glavier M, Zhang L, Gaillochet**
1613 **C, Goeschl C, et al** (2021) The receptor kinase SRF3 coordinates iron-level and flagellin dependent
1614 defense and growth responses in plants. Nat Com **13**: 4445

1615 **Prinz WA, Toulmay A, Balla T** (2020) The functional universe of membrane contact sites. Nat Rev Mol
1616 Cell Biol **21**: 7–24

1617 **Qian T, Li C, Liu F, Xu K, Wan C, Liu Y, Yu H** (2022) Arabidopsis synaptotagmin 1 mediates lipid
1618 transport in a lipid composition-dependent manner. Traffic **23**: 346–356

1619 **Radulovic M, Wenzel EM, Gilani S, Holland LK, Lystad AH, Phuyal S, Olkkonen VM, Brech A,**

Jäättelä M, Maeda K, et al (2022) Cholesterol transfer via endoplasmic reticulum contacts mediates lysosome damage repair. EMBO J. doi: 10.15252/embj.2022112677

Rizo J, Su TC (1998) C2-domains, Structure and Function of a universal Ca2+ binding Domain. J Biol Chem **273**: 15879–15882

Robe, K., Conejero, G., Gao, F., Lefebvre-Legendre, L., Sylvestre-Gonon, E., Rofidal, V., Hem, S., Rouhier, N., Barberon, M., Hecker, A., et al. (2021). Coumarin accumulation and trafficking in Arabidopsis thaliana: a complex and dynamic process. The New phytologist 229, 2062-2079. 10.1111/nph.17090.

Rowland AA, Chitwood PJ, Phillips MJ, Voeltz GK (2014) ER contact sites define the position and timing of endosome fission. Cell **159**: 1027–1041

Ruiz-Lopez N, Pérez-Sancho J, del Valle AE, Haslam RP, Vanneste S, Catalá R, Perea-Resa C, van Damme D, García-Hernández S, Albert A, et al (2021) Synaptotagmins at the endoplasmic reticulum–plasma membrane contact sites maintain diacylglycerol homeostasis during abiotic stress. Plant Cell **33**: 2431–2453

Sager R, Wang X, Hill K, Yoo BC, Caplan J, Nedo A, Tran T, Bennett MJ, Lee JY (2020) Auxin-dependent control of a plasmodesmal regulator creates a negative feedback loop modulating lateral root emergence. Nat Commun **11**: 1–10

Saheki Y, Bian X, Schauder CM, Sawaki Y, Surma MA, Klose C, Pincet F, Reinisch KM, De Camilli P (2016) Control of plasma membrane lipid homeostasis by the extended synaptotagmins. Nat Cell Biol **18**: 504–15

Salvador-Gallego R, Hoyer MJ, Voeltz GK (2017) SnapShot: Functions of endoplasmic reticulum membrane contact sites. Cell **171**: 1224.e1-1224.e1

Schauder CM, Wu X, Saheki Y, Narayanaswamy P, Torta F, Wenk MR, De Camilli P, Reinisch KM (2014) Structure of a lipid-bound extended synaptotagmin indicates a role in lipid transfer. Nature **510**: 552–555

Schindelin J, Arganda-Carreras I, Frise E, Kaynig V, Longair M, Pietzsch T, Preibisch S, Rueden C, Saalfeld S, Schmid B, et al (2012) Fiji: An open-source platform for biological-image analysis. Nat Methods **9**: 676–682

Scorrano L, De Matteis MA, Emr S, Giordano F, Hajnóczky G, Kornmann B, Lackner LL, Levine TP, Pellegrini L, Reinisch K, et al (2019) Coming together to define membrane contact sites. Nat Commun **10**: 1287

Siligato, R., Wang, X., Yadav, S.R., Lehesranta, S., Ma, G., Ursache, R., Sevilem, I., Zhang, J., Gorte, M., Prasad, K., et al. (2016). MultiSite Gateway-Compatible Cell Type-Specific Gene-Inducible System for Plants. Plant Physiol 170, 627-641.

Simon MLA, Platre MP, Assil S, Van Wijk R, Chen WY, Chory J, Dreux M, Munnik T, Jaillais Y (2014) A multi-colour/multi-affinity marker set to visualize phosphoinositide dynamics in Arabidopsis. Plant J **77**: 322–337

Simon MLA, Platre MP, Marquès-bueno, Maria M, Armengot L, Stanislas T, Bayle V, Caillaud M,

1658 **Jaillais Y** (2016) APtdIns(4)P-driven electrostatic field controls cell membrane identity and
1659 signalling in plants. Nat Plants **20;2**: 16089

1660 **Slovak R, Göschl C, Su X, Shimotani K, Shiina T, Busch W** (2014) A scalable open-source pipeline
1661 for large-scale root phenotyping of Arabidopsis. Plant Cell **26**: 2390–2403

1662 **Soboloff J, Spassova M a., Dziadek M a., Gill DL** (2006) Calcium signals mediated by STIM and Orai
1663 proteins-A new paradigm in inter-organelle communication. Biochim Biophys Acta - Mol Cell Res
1664 **1763**: 1161–1168

1665 **Song JH, Kwak S, Nam KH, Schiefelbein J, Lee MM** (2019) QUIRKY regukates root epidermal cell
1666 patterning through stabilizing SCRAMBLED to control CAPRICE movement in Arabidopsis. Nat
1667 Commun **10**: 1–12

1668 **Song L, Wang Y, Guo Z, Lam SM, Shui G, Cheng Y** (2021) NCP2/RHD4/SAC7, SAC6 and SAC8
1669 phosphoinositide phosphatases are required for PtdIns4P and PtdIns(4,5)P2 homeostasis and
1670 Arabidopsis development. New Phytol **231**: 713–725

1671 **Souza PCT, Alessandri R, Barnoud J, Thallmair S, Faustino I, Grünewald F, Patmanidis I,**
1672 **Abdizadeh H, Bruininks BMH, Wassenaar TA, et al** (2021) Martini 3: a general purpose force
1673 field for coarse-grained molecular dynamics. Nat Methods 2021 184 **18**: 382–388

1674 **Sritharan S, Versini R, Petit J, Bayer E, Taly A** (2023) Deep Learning-Based Prediction of A.
1675 thaliana's MCTP4 Structure and Exploration of Transmembrane Dynamics using Coarse-Grained
1676 Molecular Dynamics Simulations. bioRxiv 2023.08.04.552001

1677 **Stahl Y, Faulkner C** (2016) Receptor complex mediated regulation of symplastic traffic. Trends Plant
1678 Sci **21**: 450–459

1679 **Stahl Y, Grabowski S, Bleckmann A, Kühnemuth R, Weidtkamp-Peters S, Pinto KG, Kirschner**
1680 **GK, Schmid JB, Wink RH, Hülsewede A, et al** (2013) Moderation of arabidopsis root stemness
1681 by CLAVATA1 and ARABIDOPSIS CRINKLY4 receptor kinase complexes. Curr Biol **23**: 362–
1682 371

1683 **Stephani M, Picchianti L, Gajic A, Beveridge R, Skarwan E, Hernandez VS de M, Mohseni A,**
1684 **Clavel M, Zeng Y, Naumann C, et al** (2020) A cross-kingdom conserved er-phagy receptor
1685 maintains endoplasmic reticulum homeostasis during stress. Elife **9**: 1–105

1686 **Tee EE, Johnston MG, Papp D, Faulkner C** (2022) A PDLP-NHL3 complex integrates plasmodesmal
1687 immune signaling cascades. PNAS **120**: e2216397120

1688 **Thole JM, Vermeer JEM, Zhang Y, Gadella TWJ, Nielsen E** (2008) Root Hair Defective4 encodes a
1689 phosphatidylinositol-4-phosphate phosphatase required for proper root hair development in
1690 Arabidopsis thaliana. Plant Cell **20**: 381–395

1691 **Tilsner J, Linnik O, Louveaux M, Roberts IM, Chapman SN, Oparka KJ** (2013) Replication and
1692 trafficking of a plant virus are coupled at the entrances of plasmodesmata. J Cell Biol **201**: 981–995

1693 **Tilsner J, Nicolas W, Rosado A, Bayer EM** (2016) Staying Tight: Plasmodesmal Membrane Contact

1694 Sites and the Control of Cell-to-Cell Connectivity in Plants. Annu Rev Plant Biol **67**: 1–28

1695 **Tilsner J, Taliansky M, Torrance L** (2014) Plant Virus Movement. Encycl life Sci 1–12

1696 **Tran TM, McCubbin TJ, Bihmidine S, Julius BT, Baker RF, Schauflinger M, Weil C, Springer N,**
1697 **Chomet P, Wagner R, et al** (2019) Maize Carbohydrate Partitioning Defective33 Encodes an
1698 MCTP Protein and Functions in Sucrose Export from Leaves. Mol Plant **12**: 1278–1293

1699 **Tubiana T, Sillitoe I, Orengo C, Reuter N** (2022) Dissecting peripheral protein-membrane interfaces.
1700 PLoS Comput Biol. doi: 10.1371/journal.pcbi.1010346

1701 **Tylewicz S, Bhalerao RP, Petterle A, Marttila S, Miskolczi P, Azeez A, Singh RK, Immanen J,**
1702 **Mähler N, Hvidsten TR, et al** (2018) Photoperiodic control of seasonal growth is mediated by
1703 ABA acting on cell-cell communication. Science (80-) **360**: 212–215

1704 **Vaddepalli P, Herrmann A, Fulton L, Oelschner M, Hillmer S, Stratil TF, Fastner A, Hammes UZ,**
1705 **Ott T, Robinson DG, et al** (2014) The C2-domain protein QUIRKY and the receptor-like kinase
1706 STRUBBELIG localize to plasmodesmata and mediate tissue morphogenesis in Arabidopsis
1707 thaliana. Development **141**: 4139–4148

1708 **Vatén A, Dettmer J, Wu S, Stierhof YD, Miyashima S, Yadav SR, Roberts CJ, Campilho A, Bulone**
1709 **V, Lichtenberger R, et al** (2011) Callose biosynthesis regulates symplastic trafficking during root
1710 development. Dev Cell **21**: 1144–1155

1711 **Wang P, Pleskot R, Zang J, Winkler J, Wang J, Yperman K, Zhang T, Wang K, Gong J, Guan Y,**
1712 **et al** (2019) Plant AtEH/Pan1 proteins drive autophagosome formation at ER-PM contact sites with
1713 actin and endocytic machinery. Nat Commun. doi: 10.1038/s41467-019-12782-6

1714 **Wang X, Sager R, Cui W, Zhang C, Lu H, Lee J-Y** (2013) Salicylic acid regulates Plasmodesmata
1715 closure during innate immune responses in Arabidopsis. Plant Cell **25**: 2315–29

1716 **Wang Y, Perez-Sancho J, Platre MP, Callebaut B, Smokvarska M, Ferrer K, Luo Y, Nolan TM,**
1717 **Sato T, Busch W, et al** (2023) Plasmodesmata mediate cell-to-cell transport of brassinosteroid
1718 hormones. Nat Chem Biol **June**: 1–11

1719 **Wilhelm LP, Wendling C, Védie B, Kobayashi T, Chenard M, Tomasetto C, Drin G, Alpy F** (2017)
1720 STARD 3 mediates endoplasmic reticulum-to-endosome cholesterol transport at membrane contact
1721 sites . EMBO J **36**: 1412–1433

1722 **Wong LH, Levine TP, Wirtz KW, Zilversmit DB, Pagano RE, Vance JE, Bernhard W, Rouiller C,**
1723 **Prinz WA, Vihtelic TS, et al** (2016) Lipid transfer proteins do their thing anchored at membrane
1724 contact sites… but what is their thing? Biochem Soc Trans **44**: 517–27

1725 **Wozny MR, Di Luca A, Morado DR, Picco A, Khaddaj R, Campomanes P, Ivanović L, Hoffmann**
1726 **PC, Miller EA, Vanni S, et al** (2023) In situ architecture of the ER–mitochondria encounter
1727 structure. Nature **618**: 188–192

1728 **Wu H, Carvalho P, Voeltz GK** (2018a) Here, there and everywhere: The importance of ER membrane
1729 contact sites. Science (80-) **361**: 466

1730 **Wu S-W, Kumar R, Bagus A, Iswanto B, Kim J-Y** (2018b) Callose balancing at plasmodesmata. J Exp
1731 Bot **69**: 5325–5339

1732 **Yan D, Yadav SR, Paterlini A, Nicolas WJ, Petit JD, Brocard L, Belevich I, Grison MS, Vaten A,**
1733 **Karami L, et al** (2019) Sphingolipid biosynthesis modulates plasmodesmal ultrastructure and
1734 phloem unloading. Nat Plants **5**: 604–615

1735 **Yu H, Liu Y, Gulbranson DR, Paine A, Rathore SS, Shen J** (2016) Extended synaptotagmins are
1736 Ca2+-dependent lipid transfer proteins at membrane contact sites. Proc Natl Acad Sci U S A **113**:
1737 4362–4367

1738 **Zavaliev R, Ueki S, Epel BL, Citovsky V** (2011) Biology of callose (β-1,3-glucan) turnover at
1739 plasmodesmata. Protoplasma **248**: 117–130

1740 **Zhu T, Lucas WJ, Rost TL** (1998) Directional cell-to-cell communication in the Arabidopsis root apical
1741 meristem I. An ultrastructural and functional analysis. Protoplasma. doi: 10.1007/BF01280585

1742